UNIVERSITÀ DEGLI STUDI DI PADOVA

Dipartimento di Ingegneria Industriale DII
Corso di Laurea Magistrale in Ingegneria Aerospaziale

Design of sensor architecture for monitoring integrity of 3D-printed panels for extraterrestrial habitats

STUDENTE
Martina Bedendo
Matricola n° 2045220

RELATORE
Prof. Carlo Bettanini Fecia di Cossato

ANNO ACCADEMICO
2023-2024

Alla mia mamma, Patrizia,
dedico questa tesi,
il mio percorso accademico,
la mia crescita personale.
La tua forza è sempre stata anche la mia,
senza di te non ce l'avrei mai fatta.

Grazie.

Mi manchi.

Abstract

This thesis develops within the project GLAMS, Geopolymers for Lunar Additive Manufacturing And Sensing, and have the purpose to study a measurement advice that is capable of detecting a superficial or inner damage of a 3D-printed panel, generated with the additive manufacturing process.

The panel could be damage because of an hypervelocity impact with a primary debris, which comes from space, or a secondary debris, which is an ejected particle from a primary impact on the lunar surface, but the last type of debris is not fast enough to escape the Moon's gravitational field (2.4 km/s). These particles follow an elliptical trajectory around the Moon for tens of chilometers and could impact against an astronaut during extra-vehicular activity or against the "moon-house", so against the structural panel mentioned before.

This panel is made of a geopolymeric mixture and foaming agents, to best simulate a possible panel formed by regolith lunar.

For the purpose of the thesis, different types of measurement advices were examined, including capacitive sensors, resistive sensors, sensor for temperature measurement, electro-resistive sensors, the use of an Event Camera to visualize the event, and finally vibration sensors; the project is proceeding during next months, so as first material model concrete are used for simulation the impact event, both for projectile and for the target.

From impact simulations, carried out using Ansys AUTODYN software, it was possible to eliminate the temperature sensors. In fact, the simulations have shown that the temperature is not easily measurable around the point of impact, both for primary and secondary impacts. In fact an impact between a plate and a micro-meteorite, the debris, with a size of hundreds of micro-meters produces a high temperature variation at the point of impact, however it decreases rapidly a few tens of millimeters around the point of impact. So, it is not possible to insert a temperature sensor so near to the impact point to be able to measure the temperature variation.

The sensors chosen are:

- ERI (Electrical Resistivity Imaging) technology: this technology is used in civil sector to detect any fractures in the ground, in fact using a grid of electrodes embedded in the ground it is possible to measure the potential difference with a given current input. With a change in electrical resistivity in the presence of a different medium, for example the air inside a fracture, the difference in values for the potential is possible be obtained and, through use of a dedicated software, a visual feedback is obtained by generating an image (1D, 2D or 3D) of that area;

- resistive sensors: its operation is based on the presence of a grid of conductive lines, whose mutual distance is related to the resolution of the system. A control

system verifies the correct passage of current through the lines; if a line is broken, there is no current flow and it gives as output the occurrence of an impact;

- Event Camera: This type of camera detects the difference in light intensity between consecutive events, so it does not generate photos like traditional cameras. The variation is uploaded into a binary system, hence the single pixel is sent as information. It is possible to add to the main mixture some pigments, luminescent substances or pyrotechnic components in order to amplify the flash generated by the impact.

In this way it is possible to obtain a set of information on the event or not of the impact, as well as the actual degradation of the structural panel, inside and outside. The astronaut is able to understand the extent of the damage, thus to be able to carry out maintenance work or, in the worst case scenario, to replace the structural panel when it is too damaged or perforated.

Sommario

Questa tesi si sviluppa all'interno del progetto *GLAMS, Geopolymers for Lunar Additive Manufacturing And Sensing* e ha lo scopo di trovare un sensore di misura che sia in grado di dare dei *feedback* quando viene riscontrato un danneggiamento superficiale di un pannello stampato attraverso l'utilizzo dell'*additive manufacturing*, oppure quando c'è il riscontro di un danno interno al pannello.

Può essere danneggiato a causa di un impatto iperveloce di un detrito primario, ovvero che proviene dallo spazio, oppure di un detrito secondario, cioè materiale eiettato da un impatto primario con la superficie della Luna; dato che i detriti eiettati non sono abbastanza veloci per sfuggire alla forza gravitazionale della Luna (velocità di fuga 2.4 km/s) si forma una "nube. Questi *ejecta* seguono una traiettoria ellissoidale intorno alla Luna per qualche decina di chilometro, durante questo viaggio è possibile che impattino contro un astronauta durante le attività extra-veicolari oppure contro la "casa lunare", perciò contro il pannello strutturale citato precedentemente.

Il pannello strutturale è composto da una miscela di geopolimeri ed agenti schiumanti, in modo tale da simulare al meglio un possibile pannello formato da regolite lunare.

Per lo scopo della tesi sono state vagliate varie tipologie di strumenti di misura, tra cui i sensori capacitivi, sensori resistivi, sensore per la misurazione della temperatura, sensori elettro-resisitivi, l'utilizzo di una *Event Camera* per visualizzare l'evento, infine sensori di vibrazioni; inoltre il progetto è in fase di sviluppo, per cui il materiale utilizzato come modello dell'evento di impatto è il calcestruzzo, sia per quanto riguarda l'elemento impattante sia per il materiale del pannello stesso.

Dalle simulazioni di impatto, effettuate utilizzando il software *Ansys AUTODYN*, è stato possibile eliminare l'utilizzo dei sensori di temperatura. Infatti le simulazioni hanno mostrato che la temperatura non è facilmente misurabile nell'intorno del punto di impatto, sia per impatti primari sia per quelli secondari. Infatti un impatto tra una piastra ed un micro-meteorite, ovvero il detrito, grande qualche centinaio di micro-metri produce una elevata variazione di temperatura nel punto di impatto, però diminuisce drasticamente già a qualche decina di millimetro di distanza. Non è possibile inserire dei sensori di temperatura così vicini da poter misurarne la variazione.

I sensori scelti sono:

- tecnologia ERI (*Electrical Resistivity Imaging*): questa tecnologia viene utilizzata in ambito civile per rilevare eventuali fratture nel suolo, infatti utilizzando una griglia di elettrodi inseriti nel terreno è possibile misurare la differenza di potenziale con una data corrente di ingresso. Con una variazione di resistività elettrica in presenza di un mezzo differente, per esempio l'aria all'interno di una frattura, è possibile ottenere dei valori diversi per la differenza di potenziale e at-

traverso l'utilizzo di un software dedicato si ottiene un riscontro visivo generando un'immagine (1D, 2D oppure 3D) di quell'area;

- sensori resistivi: il funzionamento si basa sulla presenza di una griglia di linee conduttive, la cui distanza reciproca è correlata alla risoluzione del sistema. Un sistema di controllo verifica il corretto passaggio di corrente attraverso le linee conduttive; se una linea viene rotta, non c'è passaggio di corrente e dà come uscita l'avvenimento di un impatto;
- *Event Camera*: questo tipo di camera rileva la differenza di intensità luminosa tra istanti consecutivi, per cui non genera fotografie come le macchine fotografiche tradizionali, quindi la variazione viene tradotta in sistema binario, per cui il singolo *pixel* è inviato come informazione. Si è pensato di aggiungere al composto principale dei pigmenti, delle sostanze luminescenti oppure delle componenti pirotecniche in modo da amplificare il *flash* generato dall'impatto.

In questo modo è possibile ottenere una terna di informazioni sull'avvenimento o meno dell'impatto, nonchè l'effettivo deterioramento subito dal pannello strutturale esternamente ed internamente. L'astronauta è in grado di capire l'entità del danno, così da poter effettuare lavori di manutenzione oppure, nel peggiore dei casi, la sostituzione del pannello strutturale quando troppo danneggiato o perforato.

Contents

Chapter 1

Introduction

Creating a habitable environment on the Moon presents significant structural challenges. The construction of a "moon house" must resist at rapid impacts and potentially high-energy damage. Additionally, to keep launch costs down, it's important to use resources available *in-situ*.

One of this resource is lunar soil, comprising powdery material mixed with fragmentation elements. By incorporating additives like urea and foam elements, it is feasible to use the powder soil for producing 3D-printed panels that will be the primary building material for lunar infrastructures.

The lunar environment is not suitable for humans, there are no atmosphere, solar and space radiations are not shielding by the moon-atmosphere, the temperature fluctuates significantly between moon-day and moon-night, meteoroids fall on the lunar surface and they could impact against astronauts during extra-vehicular activity but also against the "moon-house" structural panels. So, the damage and the integrity of panels have to be controlled and, in case, the astronaut has to perform maintenance and repair any potential hazards.

For having an alert of the damage, a selection among different measurement advices has been made, choosing those most suitable for the purpose of the entire GLAMS project: for studying the superficial and inner integrity of the 3D-printed panel, and also for using an *in-situ* approach.

1.1 GLAMS project

The acronym GLAMS stands for Geopolymers for Lunar Additive Manufacturing and Sensing, so this project has the purpose of create structural panels for a lunar outpost using an *In-Situ* Resource Utilization approach (ISRU). The aim is to build an infrastructure made by geopolymeric panels based on lunar regolith, which panels are created by additive manufacturing process; in this way, it will be possible to use the in situ resources, such as the lunar soil.

The lunar environment forces the panels design to be adapted to low gravity, low surface pressure, high gradients of temperature, long period of night and day, high solar radiation and frequent hypervelocity impacts of micrometeorites.

The GLAMS project is conceived as a proof-of-concept for the creation of buildings in lunar environment, in which it is expected the medium-scale production of specific sensorized structural units.

In the end, the final objective is to develop an additive manufacturing process that allows the automated creation of sensorized structural units for building infrastructures in extra-terrestrial environment, these structures will be 3D-printed panels and also will having thermal insulation properties thanks to a porosity gradient along the thickness. The production process involves taking full advantage of in situ resources available.

1.2 Geopolymeric panels

To create materials that have structural properties, the main approaches to develop cohesive properties among regolith particles are:

- high-temperature sintering of particles;
- addition of a binder;
- direct reaction of the particles in aqueous solution;

The last one involves the use of regolith for the production of geopolymers, which are alternative binders created by the reaction of aluminosilicate powders in alkaline solution. In this high pH solution, the solid particles are dissolved and ionic species are formed, at super saturation condition these species sink forming new aluminosilicate phases, which give cohesive properties [22]. To obtain porous geopolymers it can be add foam to the base material, so for the creation of foamed slurries[1] there are three main approaches:

- mixing liquid foams stabilized by foaming agents with cement mixture;
- addition of foaming agent into cement mixture and subsequent generation of foam;
- addition of porous elements to cement mixture, which produce gas through chemical reactions;

---

[1] Slurry: a slurry is a fluid mixture of a liquid (typically water) with suspended solids. It behaves like a viscous fluid, semi liquid material. Common examples of slurries include muds and cements.

In the first and second method [3], the foam is produce by the insufflation of compressed gas or ventilation [4].

In the last one, it is possible to incorporate porous elements into the slurry. The main elements are aluminium and metallic silicon to produce porous geopolymers on the Moon [6], because the lunar surface is rich of these elements and it is possible to produce oxygen from the electrolysis of molten regolith, which should be the "compressed gas", in agreement with the ISRU approach. The exothermic reaction between water and metallic silicon or aluminium produces hydrogen, this element could be use in fuel cells to produce water and energy for astronauts.

Recent studies highlight the possibility to use urea like additive in the geopolymeric material [19, 20].

Another challenge is to be able to create 3D-printed structural panel with these new porous material, this technique is called properly additive manufacturing. Therefore, the material has to resist direct extrusion without collapse and without lose the porosity gradient.

The additive manufacturing is a group of techniques for producing three-dimensional parts, based on the superposition of layers that follow a digital model. It is possible to create parts with complicated shape, which is not possible with classical processes.

Since this project has the purpose of building on the Moon, the additive manufacturing must overcome the lunar environment, like:

- low gravity: it is possible to create angular shapes, thanks to the low deformation that occurs; then the cement mixture has a mechanical resistance proportional to gravity [23], but foam materials have a positive reaction to low gravity. So low gravity could be an advantage for the additive manufacturing process;

- no atmosphere: vacuum condition, no wind, no rainfall; in this case the porosity increases thanks to vacuum (advantage for the purpose to have a porous panel), at the expense of mechanical properties (disadvantage). On the other hand, micrometeorites impacts often occur (disadvantage), so it is necessary to know the damage caused by impacts and to create an impact resistant material;

- no magnetic field: high flux of cosmic rays and UV rays (disadvantage), for shielding from these emissions it is required to study the right thickness of the panel;

- gradient of temperature: the material has to be able to resist at freeze-thaw cycles and to insulate thermally the astronauts' habitat.

1.3 Aim of this thesis

The purpose of this thesis is to define an architecture design for monitoring integrity of the panels, so the goal is to identify an optimal configuration of measuring devices that will be inside or outside the element for detecting hypervelocity impacts, locating impact area and determining the degradation of the panel.

Therefore, different types of devices were examined, based on *Ansys AUTODYN* software for the simulations the temperature sensors have been excluded. The model used in the simulations is P-α model for the panel simulant material and Smoothed-Particle hydrodynamics (SPH) for simulating the material deformation during hypervelocity impact. These concepts will be describe in more detail in Chapter 4.

This research is funded and supervised by the Italian Space Agency (*Agenzia Spaziale Italiana, ASI*) in the framework of the Research Day *Giornate della Ricerca Spaziale* initiative through the contract no. ASI-2023-6-U.0.

Chapter 2

Simulants for lunar regolith

Given the small quantity of lunar regolith samples, it is necessary to produce simulants of this material. Simulants are powders that reproduce particle size distribution, chemical and mineralogical composition of the real lunar regolith.

The simulant Lunar Mare Simulant (LMS-1), produced by Exolith, was chosen thanks to the similarity with the one of Johnson Space Center (JSC), to replicate the properties of regolith in lunar maria and also because Exolith produces simulants continuously, homogeneously and in large volumes.

In table 2.1, the chemical analysis of some considered simulants is reported.

In the end, LMS-1D and JSC-2A were chosen. LMS-1D has a finer grain size, this improves the reactivity of the powders. These samples were subjected to different tests in order to quantify the mineralogical phases and other properties, in particular to understand the amount of amorphous fraction present. In fact, more amorphous fraction is correlated with the better reactivity in aqueous solution, since the amorphous state is related to a high Gibbs free energy compared to the crystalline one.

Table 2.2 represents the mineralogical phases present into LMS-1D and JSC-2A.

Unfortunately, JSC-2A is difficult to get in large volumes, but LMS-1D is easy to have, so metakaolin was added to LMS-1D to make this simulant more similar to JSC-2A in terms of quantity of amorphous material.

In figure 2.1, there are some hardened samples of simulant regolith.

During the missions on the Moon, many samples were obtain from different areas (see figure 2.2). These samples vary from each other by the different quantities of pyroxene, olivine, plagioclase and iron and titanium oxides, as well as amorphous volcanic glass.

Ultimately, lunar regolith has a non-homogeneous composition linked to the sampling area, so the simulants are created from mean properties of lunar regolith. For this, it is necessary to find spots that have the correct quantity of amorphous material, in order to maximize reactivity in aqueous solution.

This project is in progress, so there will be further developments in the coming

Wt. %	**LMS-1**	**Exolith**	**LMS-1D**	**Exolith**	**DNA**	**EAC**	**JSC**
SiO_2	48.6	44.2	47.2	45.9	53.2	43.3	46.0
TiO_2	2.1	3.5	3.2	3.6	0.8	2.2	1.8
Al_2O_3	12.2	11.9	13.1	12.4	17.8	11.6	16.1
Fe_2O_3	9.8	11.5	9.9	8.6	6.9	12.9	13.0
MnO	0.2	0.2	0.2	0.2	0.1	0.2	0.2
$Mg0$	17.1	17.1	15.9	16.8	2.7	14.0	8.3
CaO	7.5	8.6	7.5	7.0	8.1	11.0	9.7
Na_2O	1.5	0.9	1.7	1.7	3.5	2.8	3.1
K_2O	0.4	0.4	0.7	0.7	6.1	1.0	0.8
P_2O_5	0.2	0.9	0.2	0.2	0.4	0.7	0.7
Tot	99.6	99.2	99.7	98.1	99.6	99.7	99.7
$L.O.I.$	0.6		1.1	0.9	1.7	3.0	0.0

Table 2.1. Chemical analysis of some considered simulants.

Wt.%	**LMS-1D**	**JSC**
Plagioclase	37.0	37.6
Pyroxene	27.0	6.1
Olivin	14.1	14.3
Others	11.4	0.3
Amorphous	10.5	41.7

Table 2.2. Mineralogical phases present into LMS-1D and JSC-2A. JSC-2A has an amorphous phase greater than the one of LMS-1D.

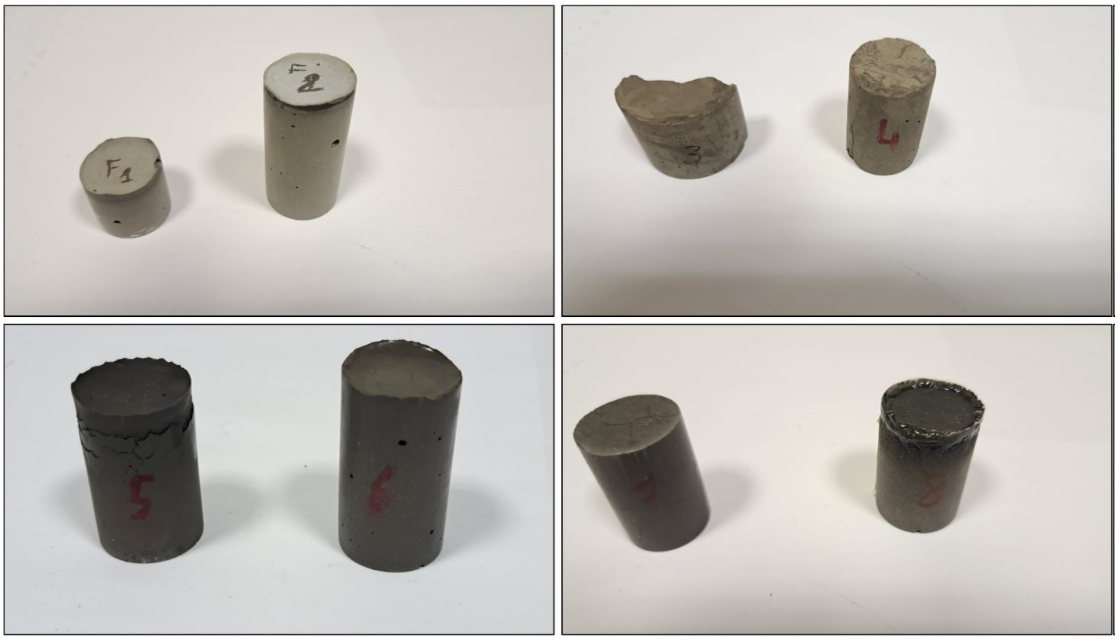

Figure 2.1. Hardened samples of simulant regolith with a diameter of 2 cm.

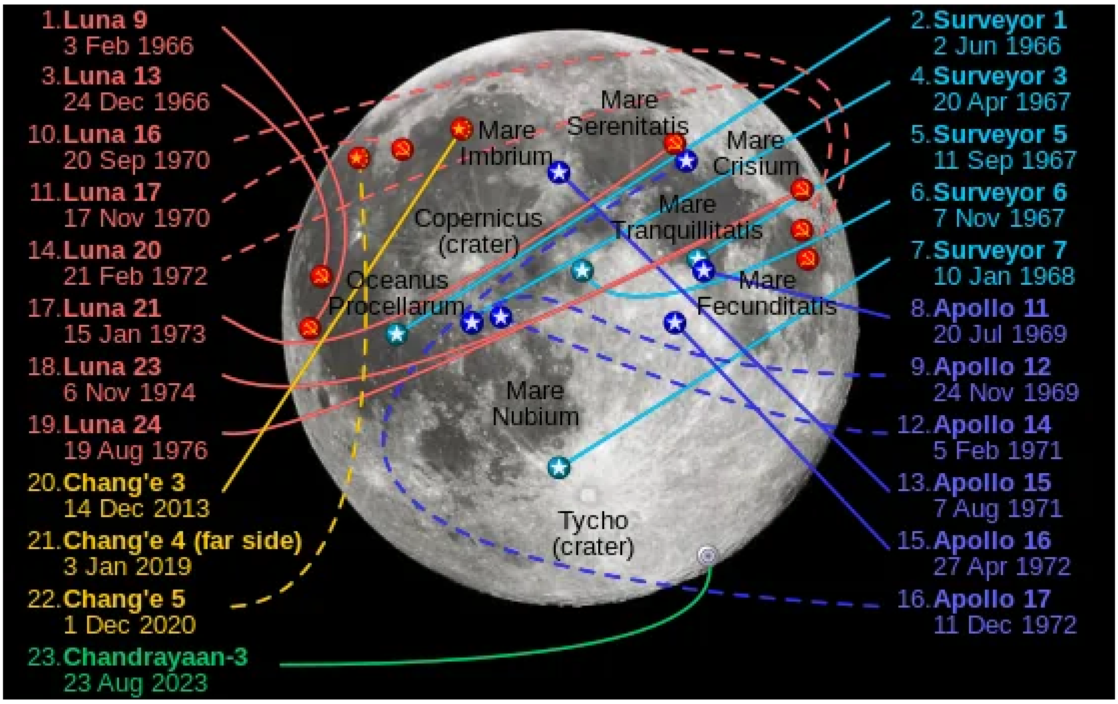

Figure 2.2. Different sites where regolith samples were collected during lunar missions.

months. The information in this section are taken from the technical report of the first progress meeting during January 2024.

Chapter 3

The Moon

This section describes lunar characteristics that are important for GLAMS project, so for having more information about Moon log into NASA website reported in bibliography [17].

Due to a very weak atmosphere (exosphere), there is not protection from Sun's radiation or from meteoroid impacts.

Moreover, meteoroids, asteroids and comets strike the surface of the Moon producing several craters. In figure 3.1 it is shown the different shapes of moon craters, it is possible to have a simple crater, a crater transition between simple and complex one, a central peak crater or a central peak basin crater; for having more details about the creation of this shapes read chapter 4 of Lunar Sourcebook [10]. Also in figure 3.2 is shown a schematic view of the shapes mentioned above.

Over billions of years, these impacts have pulverized the surface soil and rocks producing the lunar regolith, which is a charcoal-grey powder with some rocky debris. A layer of fragmented rocks is beneath the regolith and it is called megaregolith.

The upcoming chapter will focus on providing a comprehensive overview of hypervelocity impacts with a specific emphasis on their effects on the Moon.

3.1 Soil and lunar regolith

The idea of regolith is a terrestrial concept, which is also use for the Moon. It is possible to define it as *"a general term for the layer or mantle of fragmental and unconsolidated rock material, whether residual or transported and of highly varied character, that nearly everywhere forms the surface of the land and overlies or covers bedrock. It includes rock debris of all kinds, [including] volcanic ash . . ."* from Bates and Jackson, 1980.

The lunar regolith is created through the formation of powder rocks resulting from impacts by both large and small meteoroids, combined with the influence of solar and cosmic particles on the lunar surface. Due to the shock over-pressures and heat, generated by impact cratering events, a considerable amount of pulverized material undergoes melting and welding processes.

A consequence of this event is the formation of *breccias* (fragments of rocks) and impact melt rocks, contributing considerably to the complexity of the regolith.

On the Moon there are mainly two areas: maria and highlands, in that sites the thickness of lunar regolith might vary from few meters (4-5 meters in maria) to ten meters (10-15 meters in highlands).

Therefore, regolith will be the basic material to build a moon base, thanks to its superficial, unconsolidated and fine-grained nature. On the other hand, it becomes evident that the regolith varies significantly from one region to another, making it challenging to replicate the characteristic features of this element across the entire lunar surface.

Ideally the stratigraphy of the regolith consists of two zones figure 3.3:

- a near-surface reworked zone, usually spanning a few to tens of centimetres, where all layers have been homogenized or mixed together, regolith;
- a sequence of slabs where the original layering remain undisturbed, megaregolith.

Optical studies on lunar samples, from missions landed on the Moon in figure 2.2, reveal the basic particles of regolith shown in figure 3.4:

- mineral fragments,
- pristine crystalline rock fragments,
- breccia fragments,
- glasses of various kinds,
- agglutinates[1], the distinctive lunar constructional particles.

For instance, the samples collected during missions such as Apollo 11, 12, Luna 16 and 24 show an abundance of mare-derived basaltic rock fragments, featuring mafic minerals like pyroxene and olivine. These missions specifically targeted maria regions.

Conversely, samples from Apollo 16 and Luna 20, which were landed in highland areas, reveal the prevalence of highland-derived lithic fragments and plagioclase feldspar.

Furthermore, samples from missions that landed in intermediate regions show characteristics that fall between those of maria and highland samples, underscoring the different nature of lunar regolith across different sites, figure 3.5.

---

[1] Agglutinates: it is formed by soil grain and glass bonded each other, the glass is produced by melting the lunar soil. Due to these reasons, agglutinates often replicate the composition of the soils from which they originated.

Ultimately, the chemical data indicates significant variations in the composition of samples from different regions. In each region, the rocks of the soil underwent processes such as shattering, pulverization, milling and mixing with other elements; these processes have led to a various range of compositions across the regions of samples.

This is a challenge in assessing the average chemical properties of regolith to develop an accurate Earth simulant for testing both additive manufacturing processes and foaming.

For having more details about the characteristics of lunar regolith read the chapter 7 of Lunar Sourcebook [15].

3.2 Temperature

The temperature on the Moon ranges from 127°C in full Sun to -173°C in darkness.

This is a challenge for the *in-situ* creation of simulant regolith panels and for the measurement devices that will be use. In fact, the panel material could freeze before or during extrusion, so it is necessary to heat it up.

Certainly an aspect not to be overlooked.

3.3 Radiative environment and shielding

Solar wind, solar flares and galactic cosmic rays arrive on the surface of the Moon without losing energy. The variable energies of these particles are reflected in the depth they can reach within lunar soil, figure 3.6.

Specifically, **solar wind particles**, with an average energy of 1 keV/amu (atomic mass unit), penetrate about 150 nm (0.15 µm) into lunar soil.

Solar flare particles, from 104 to 108 eV/amu, can breach lunar soil to depths ranging from a few millimetres to tens centimetres. These two types of particle could be called Solar Particle Events, SPE.

On the other hand, **galactic cosmic rays** (GCR), which boast energies exceeding 1 GeV/amu, can penetrate the soil up to about 1 meter. Hence, the priority is given to shielding against this type of radiation.

These data is taken from Chapter 7 of Lunar Sourcebook [15]. Also in figure 3.6 there are summarized the energy and the damage of the radiations reaching the lunar surface.

The interaction between radiation fluxes and regolith results in a significant *albedo* radiation, rich in neutrons, constituting approximately 33% of the total absorbed dose [34].

Therefore, the protective measures targets are the radiations from deep space and the albedo one. Hydrogen and lithium shields prove to be the most effective protective elements against GCR due to their low count of protons and neutrons, minimizing potential targets for incident radiation that could generate secondary neutrons.

In figure 3.7, the effective dose of GCR radiation is represented in relation to the variable thickness of the shielding. It is essential to note that a lunar regolith shield is comparable to an aluminium one, rendering it ineffective against this type of radiation.

Comparing different shields can be achieved by utilizing the shielding thickness in grams per square centimeter (g/cm^2), figure 3.8. This allows the determination of panel thickness based on the material density. Assuming a density of 3 g/cm^3 and a panel thickness of 1 m (100 cm), the shielding thickness (s.t.) is calculated as follows:

$$s.t. = thickness \cdot density = 100cm \cdot 3g/cm^3 = 300g/cm^2$$

With a 1-meter thick panel, the annual ambient dose rate can be maintained below 300 mSv/yr. This is crucial, considering the maximum recommended dose for an astronaut's career, which is 600 mSv [30].

3.4 Micro-meteoric environment

The lunar soil undergoes frequent bombardment by micro-meteoroids from space due to the absence of atmosphere. These are known as primary impacts. When a micro-meteoroid strikes the surface, it generates an ejecta flow from the crater, potentially causing secondary impacts in the surrounding area, which could be 3 or 4 orders of magnitude greater than primary flux with the same mass [8].

The cumulative mass of micro-meteoroids involved in primary impacts is more or less 1.8×10^6 kg per year, with a peak mass of around 1.5×10^{-5} g and a diameter of 220 μm, while the average impact velocity is 13.3 km/s [33].

Due to primary impact, jetting of ejecta occurs, producing a wave of melted and vaporized material. This material is ejected with low angles with respect to the horizontal and could have higher speed than impactor element [28].

Considering the conclusions of Vanzani, it becomes evident that estimating the risk to lunar infrastructure is challenging due to limited understanding of micro-meteoroid fluxes in the lunar close area. Surely, it is necessary to recognize that achieving zero risk is improbable, so it is necessary to building proper protection for long-term infrastructures; the major effect is the abrasion of the surface material due to secondary flux during time, therefore maintenance of the infrastructures is an important issue.

Although experiments shows that the majority of ejecta has a speed less than 2.4 km/s, which is the lunar escape velocity [8].

Unable to escape the gravitational force of the moon, the ejecta follow an elliptical trajectory and fall back on the surface, during this "jump" it is possible that debris impact against a human infrastructure, vehicle or astronaut. The reachable distance is calculated by the following equation [8]:

$$R = 2 \cdot r \cdot \tan^{-1}\left(\frac{\overline{V_e}^2 \cdot \sin\theta \cdot \cos\theta}{1 - \overline{V_e}^2 \cdot \cos^2\theta}\right) \tag{3.1}$$

With θ included (or equal) from 0 and $\pi/2$ and it is the angle of ejection respect to the local horizontal, $\overline{V_e}^2 = (V_e^2)/(r \cdot g_0)$, V_e is the ejection velocity, g_0 the lunar surface gravitational acceleration $(1.62 \times 10^{-3}\ \mathrm{km/s^2})$ and r lunar radius $(1.74 \times 10^3\ \mathrm{km})$.

While the maximum altitude:

$$h_{max} = r \cdot \left(\frac{\overline{V_e}^2 - 1 + \sqrt{1 - \overline{V_e}^2 \cdot (2 - \overline{V_e}^2) \cdot \cos^2\theta}}{2 - \overline{V_e}^2}\right) \tag{3.2}$$

During test on an impact between a basalt slab and an aluminium sphere with a velocity of 6.25 km/s, Donald have demonstrated that the ejecta's velocity decays quickly and the main mass of debris, that leaves the crater, has velocities less than 0.5 km/s and an inclination greater than 45° (θ angle).

The figure 3.9 represents, in logarithmic scale, m/m_p versus the range in km or the maximum altitude (km), where m is the cumulative ejected mass normalized with m_p that is the projectile mass; so it represents the distribution above the lunar surface of the mass ejected from craters in basalt.

The 90% of the ejecta will not exceed an altitude of 10 km and a radius of 30 km, but taking into account the 99% these results increase, respectively, to 30 and 150 km. The last 1% is possible that includes the ejecta able to escape the lunar gravitational field, so they are faster than 2.4 km/s.

The experiments done by Donald were between an aluminium projectile against a slab of basalt, but the lunar surface is made by powder and little fragment, as said in the previous section 3.1 and micro-meteoroids are not just made of aluminum. So the dimension and velocities of real ejected particles could be smaller than Donald ones, these effects reduce the risk and damage due to an impact.

It is possible to say that there is a "debris atmosphere" on the Moon from the surface to 30 km altitude, and the ejecta flux is larger than interplanetary one by a factor of 1800 to 60000 [5].

Combining the low speed and the small size, even though the quantity of debris is more than primary impact, data indicate that the danger for an astronaut during EVA (extra-vehicular activity) is almost the double that of considering only primary meteoroids [5], also the real risk of perforation is smaller than the one calculated with basalt slab.

For the calculation of total mass excavated from a crater and launched at speed v or larger, it is possible to use the following equation:

$$\frac{M(>v)}{m} = K \cdot \left(\frac{v}{U}\right)^{-B} \tag{3.3}$$

With m the micro-meteoroid mass, U its velocity, an impact inclination of 90° respect to the local horizontal, $M(> v)$ the total mass that leave the surface at a velocity of v or bigger [11]. This is also the mass reaches a distance r from crater or greater.

Thanks to the last equation, it is possible to estimate the diameter d (mm) of the ejecta for typical lunar soil and the number of particles N with the diameter equal or greater than d, figure 3.10; one can observe that the 90% of the particles have a diameter smaller than 1 mm [5].

Also, it can be plotted the penetrating flux versus the critical kinetic energy for the penetration of an astronaut suit [5], figure 3.11. This shows that the risk of penetration is smaller for the ejecta from lunar soil than the ones from basalt slab, with a reduction factor of 6 to 12.

Because of the challenges in creating a reliable simulant of the lunar soil, it is possible to use in first approximation basalt for experiments and simulations, but the results will need to be reviewed regarding the direct application to the lunar surface. At last, the calculated risk of an impact on basalt slab is greater than the actual risk associated with an impact on lunar soil, thanks to the characteristic of the soil to be dusty and not solid like basalt.

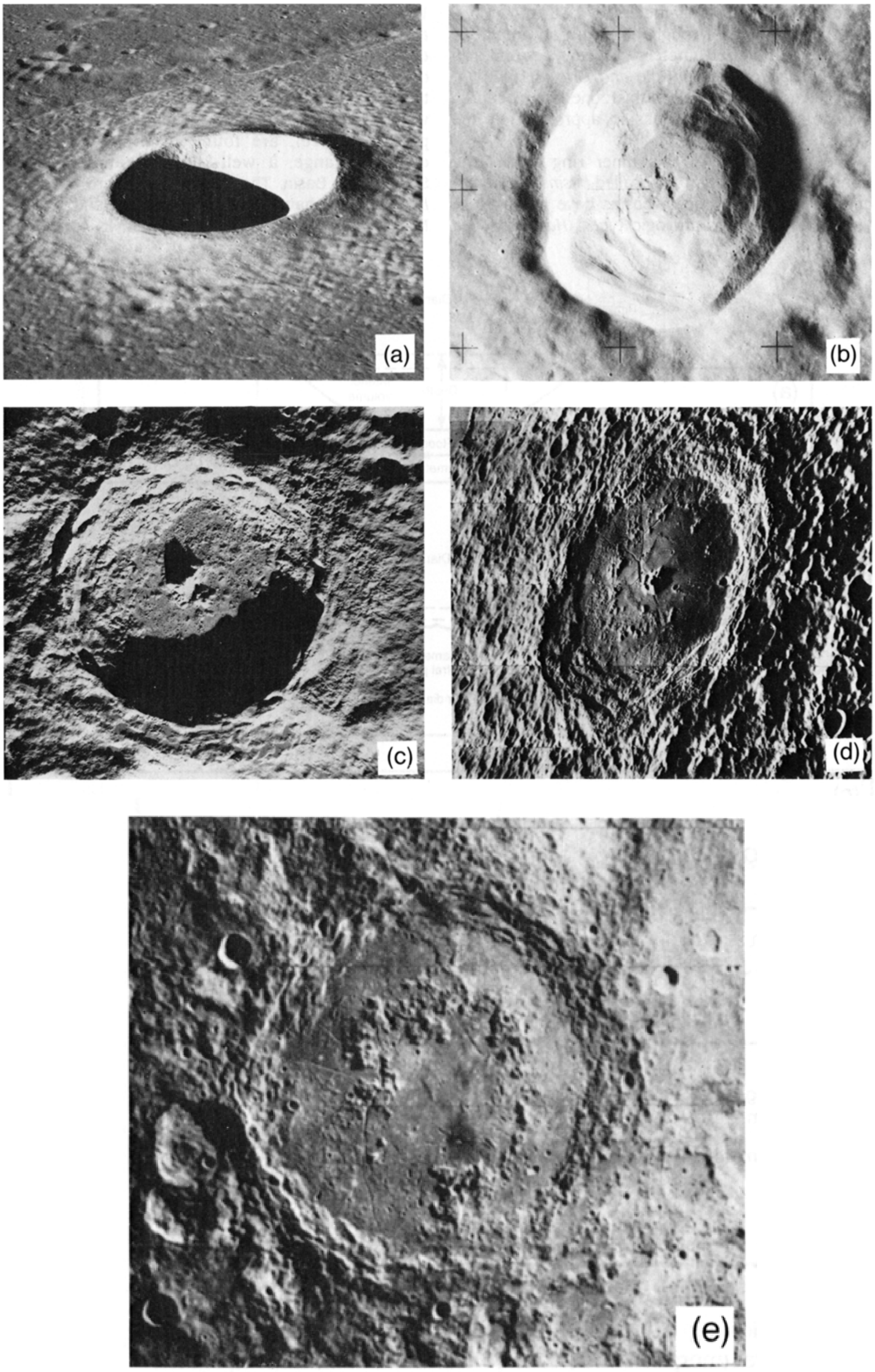

Figure 3.1. The shapes of craters on the Moon are shown in this imagine: a. Simple crater; b. Crater transitional between simple and complex morphologies; c. Central peak crater; d. Central peak basin.

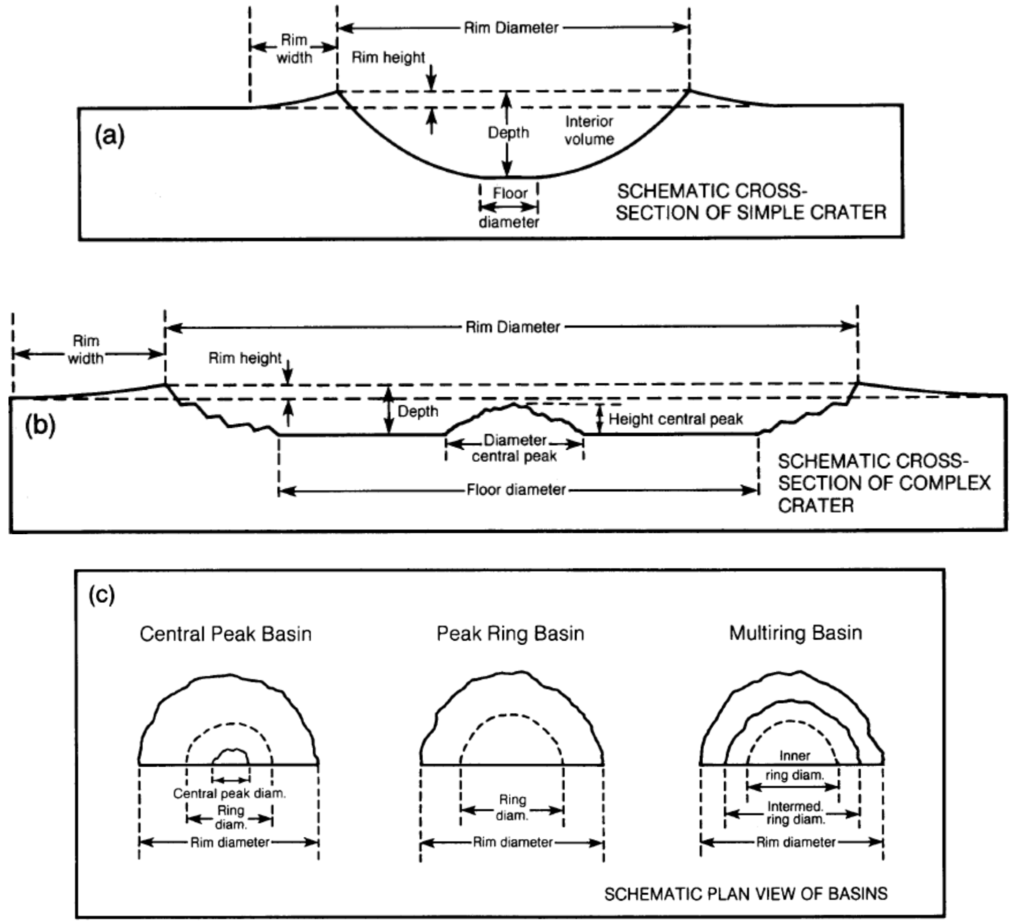

Figure 3.2. The representation of a schematic assessment of lunar impact structures, representing principal morphological elements: a. Simple crater; b. Complex central peak crater; c. Various basins [10].

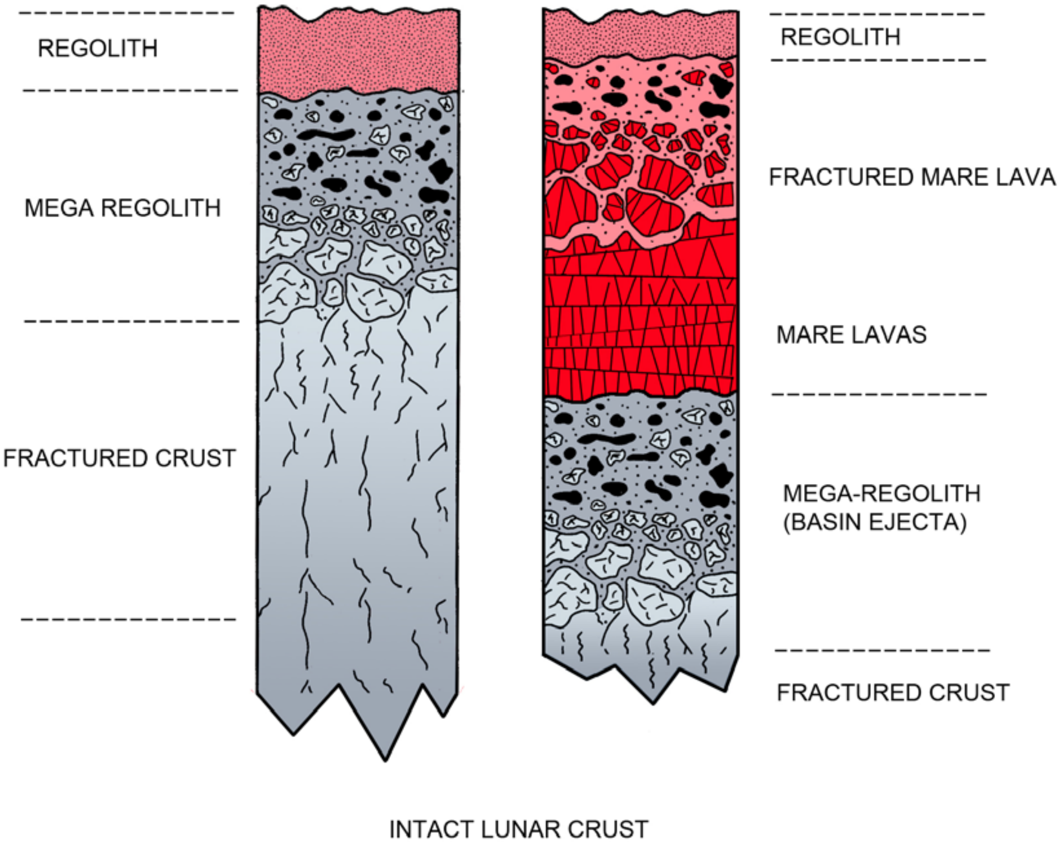

Figure 3.3. The stratigraphy of lunar soil: on top, there is regolith coating, which consists of homogenized powder layer; below there is megaregolith, which is formed by slabs and fragments of the original layering [21].

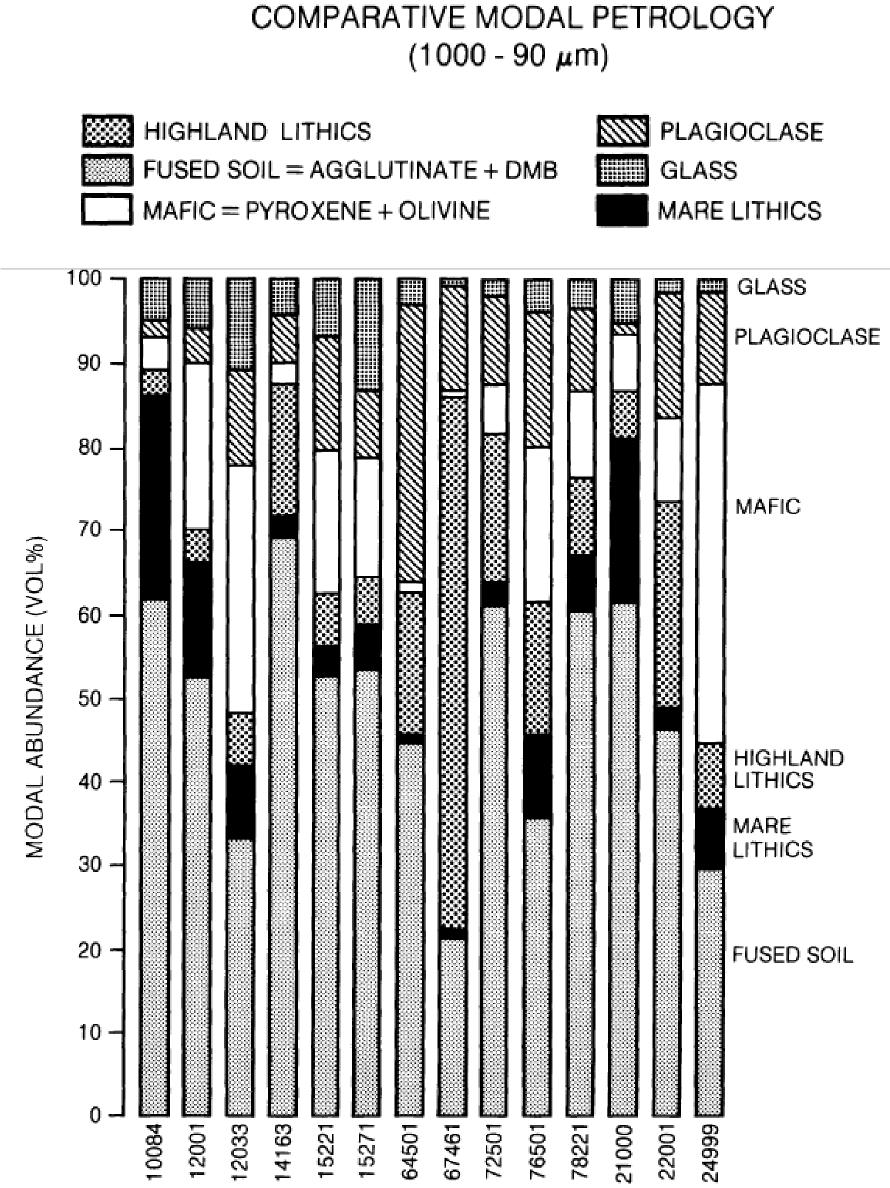

Figure 3.4. Modal (volume %) abundances of principal particle types in lunar regolith samples. This diagram distinguishes among mare lithics, highland lithics, single mineral, pyroxene, olivine, plagioclase, glass and fused soil (agglutinates and dmb—Dark Matrix Breccia). Soil samples are from Apollo 11 (10084), Apollo 12 (12—), Apollo 14 (14163), Apollo 15 (15—), Apollo 16 (6—-), Apollo 17 (7—-), Luna 16 (21000 and 22001), and Luna 24 (24999).

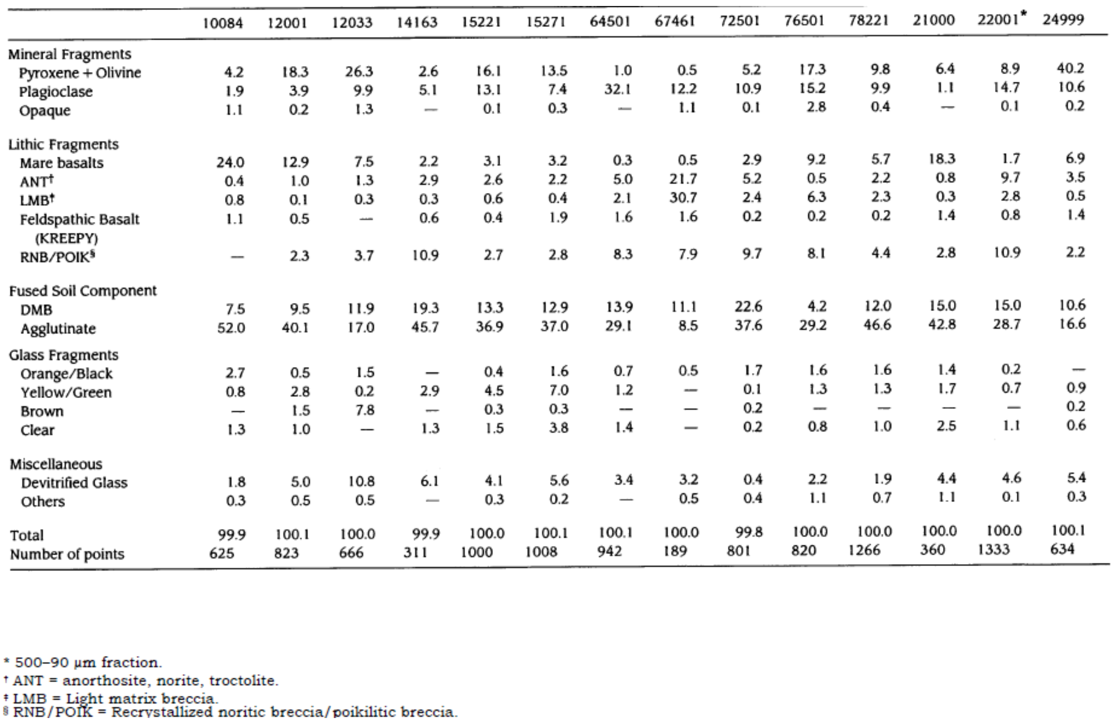

	10084	12001	12033	14163	15221	15271	64501	67461	72501	76501	78221	21000	22001*	24999
Mineral Fragments														
Pyroxene + Olivine	4.2	18.3	26.3	2.6	16.1	13.5	1.0	0.5	5.2	17.3	9.8	6.4	8.9	40.2
Plagioclase	1.9	3.9	9.9	5.1	13.1	7.4	32.1	12.2	10.9	15.2	9.9	1.1	14.7	10.6
Opaque	1.1	0.2	1.3	—	0.1	0.3	—	1.1	0.1	2.8	0.4	—	0.1	0.2
Lithic Fragments														
Mare basalts	24.0	12.9	7.5	2.2	3.1	3.2	0.3	0.5	2.9	9.2	5.7	18.3	1.7	6.9
ANT†	0.4	1.0	1.3	2.9	2.6	2.2	5.0	21.7	5.2	0.5	2.2	0.8	9.7	3.5
LMB‡	0.8	0.1	0.3	0.3	0.6	0.4	2.1	30.7	2.4	6.3	2.3	0.3	2.8	0.5
Feldspathic Basalt (KREEPY)	1.1	0.5	—	0.6	0.4	1.9	1.6	1.6	0.2	0.2	0.2	1.4	0.8	1.4
RNB/POIK§	—	2.3	3.7	10.9	2.7	2.8	8.3	7.9	9.7	8.1	4.4	2.8	10.9	2.2
Fused Soil Component														
DMB	7.5	9.5	11.9	19.3	13.3	12.9	13.9	11.1	22.6	4.2	12.0	15.0	15.0	10.6
Agglutinate	52.0	40.1	17.0	45.7	36.9	37.0	29.1	8.5	37.6	29.2	46.6	42.8	28.7	16.6
Glass Fragments														
Orange/Black	2.7	0.5	1.5	—	0.4	1.6	0.7	0.5	1.7	1.6	1.6	1.4	0.2	—
Yellow/Green	0.8	2.8	0.2	2.9	4.5	7.0	1.2	—	0.1	1.3	1.3	1.7	0.7	0.9
Brown	—	1.5	7.8	—	0.3	0.3	—	—	0.2	—	—	—	—	0.2
Clear	1.3	1.0	—	1.3	1.5	3.8	1.4	—	0.2	0.8	1.0	2.5	1.1	0.6
Miscellaneous														
Devitrified Glass	1.8	5.0	10.8	6.1	4.1	5.6	3.4	3.2	0.4	2.2	1.9	4.4	4.6	5.4
Others	0.3	0.5	0.5	—	0.3	0.2	—	0.5	0.4	1.1	0.7	1.1	0.1	0.3
Total	99.9	100.1	100.0	99.9	100.0	100.1	100.1	100.0	99.8	100.0	100.0	100.0	100.0	100.1
Number of points	625	823	666	311	1000	1008	942	189	801	820	1266	360	1333	634

* 500–90 µm fraction.

† ANT = anorthosite, norite, troctolite.

‡ LMB = Light matrix breccia.

§ RNB/POIK = Recrystallized noritic breccia/poikilitic breccia.

Figure 3.5. Modal (vol.%) abundance data for particles in the 1000–90 µm size fraction of representative soils from each mission. Soil samples are from Apollo 11 (10084), Apollo 12 (12—), Apollo 14 (14163), Apollo 15 (15—), Apollo 16 (6—-), Apollo 17 (7—-), Luna 16 (21000 and 22001), and Luna 24 (24999). This table illustrates the variance among samples of the same element collected from different missions and areas.

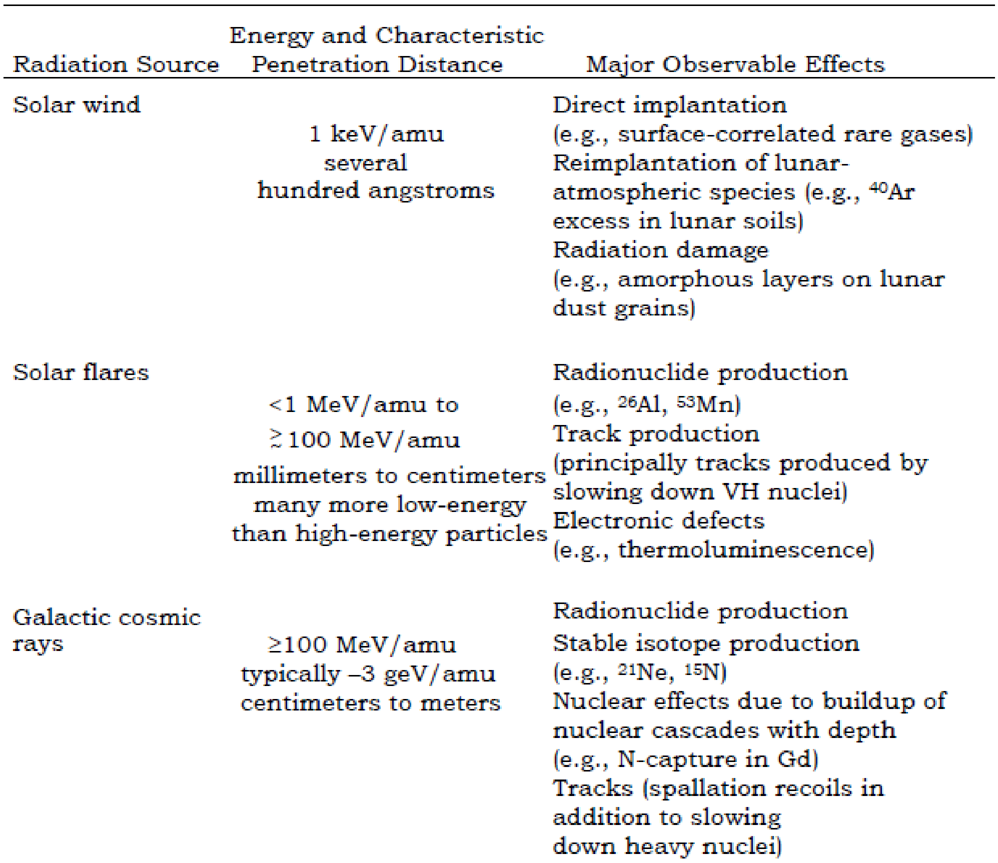

Radiation Source	Energy and Characteristic Penetration Distance	Major Observable Effects
Solar wind	1 keV/amu several hundred angstroms	Direct implantation (e.g., surface-correlated rare gases) Reimplantation of lunar-atmospheric species (e.g., ^{40}Ar excess in lunar soils) Radiation damage (e.g., amorphous layers on lunar dust grains)
Solar flares	<1 MeV/amu to $\gtrsim$100 MeV/amu millimeters to centimeters many more low-energy than high-energy particles	Radionuclide production (e.g., ^{26}Al, ^{53}Mn) Track production (principally tracks produced by slowing down VH nuclei) Electronic defects (e.g., thermoluminescence)
Galactic cosmic rays	≥100 MeV/amu typically –3 geV/amu centimeters to meters	Radionuclide production Stable isotope production (e.g., ^{21}Ne, ^{15}N) Nuclear effects due to buildup of nuclear cascades with depth (e.g., N-capture in Gd) Tracks (spallation recoils in addition to slowing down heavy nuclei)

Figure 3.6. The most important characteristics and effects of solar wind, solar flares and galactic cosmic rays are here reported [15].

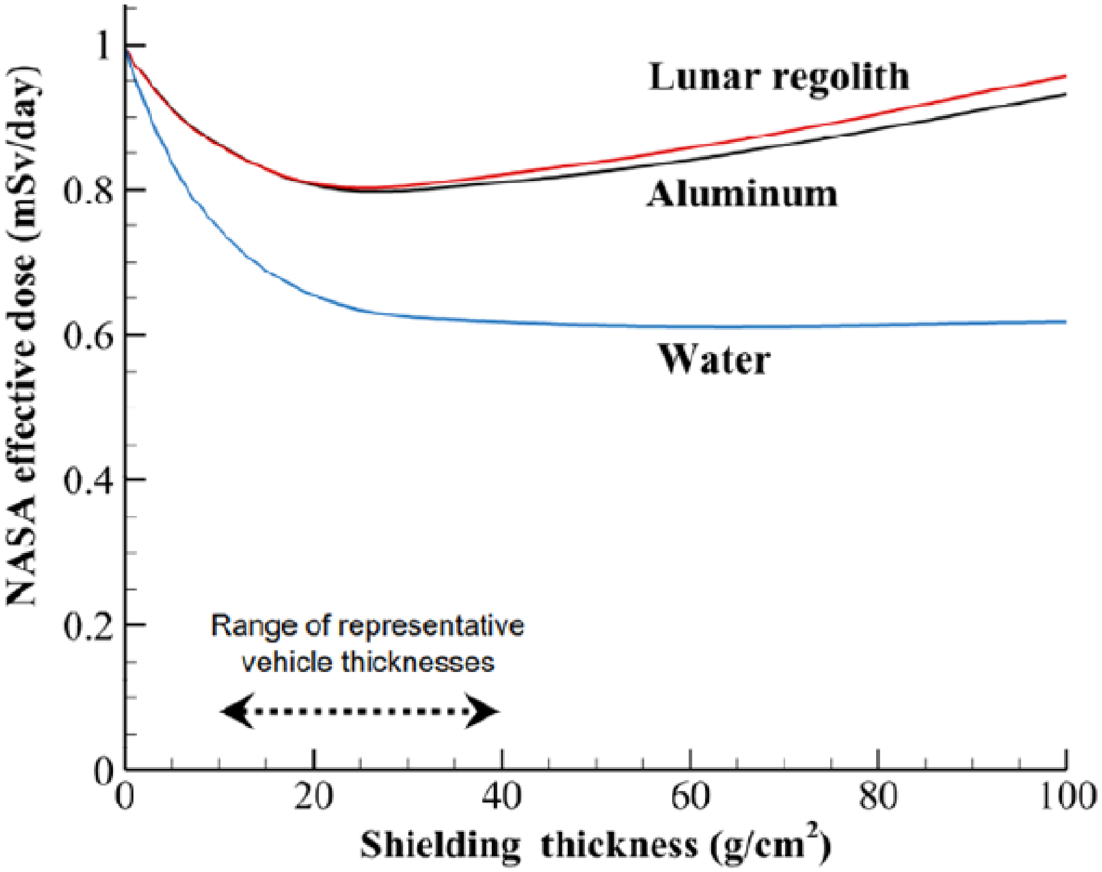

Figure 3.7. The effective dose of GCR versus the thickness of the shield is shown in this figure. The lunar regolith shield is comparable with an aluminium one, so it is not effective for this type of radiations.

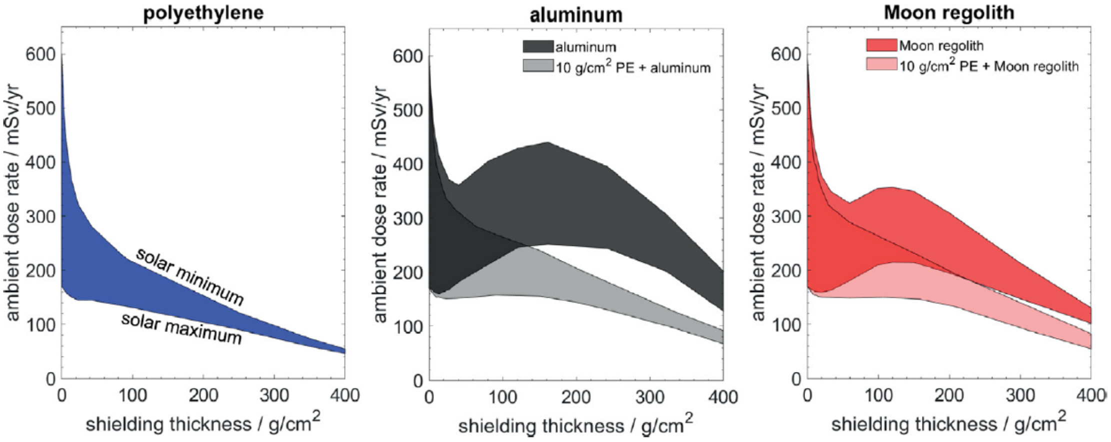

Figure 3.8. Annual ambient dose rate (mSv/yr) versus the thickness of the shielding (g/cm^2) for material like polyethylene, aluminium and lunar regolith. These graphs show the value of GCR corresponding to a solar minimum (upper line) and a maximum (bottom line); for aluminium and lunar regolith there are also values for a different configuration: principal element + two internal layers of polyethylene [9].

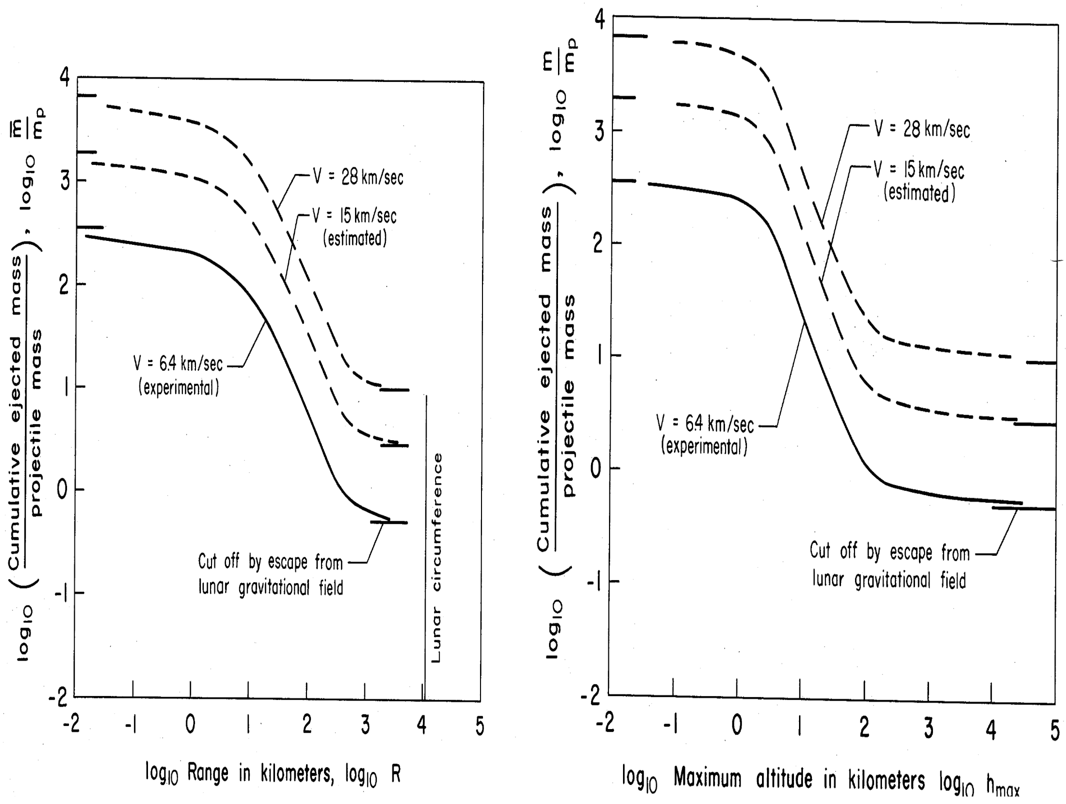

Figure 3.9. With a logarithmic scale, the graph on the left represents the m/m_p versus the range (km); the right one represents the m/m_p versus the maximum altitude. Where m is the cumulative ejected mass normalized with m_p that is the projectile mass.

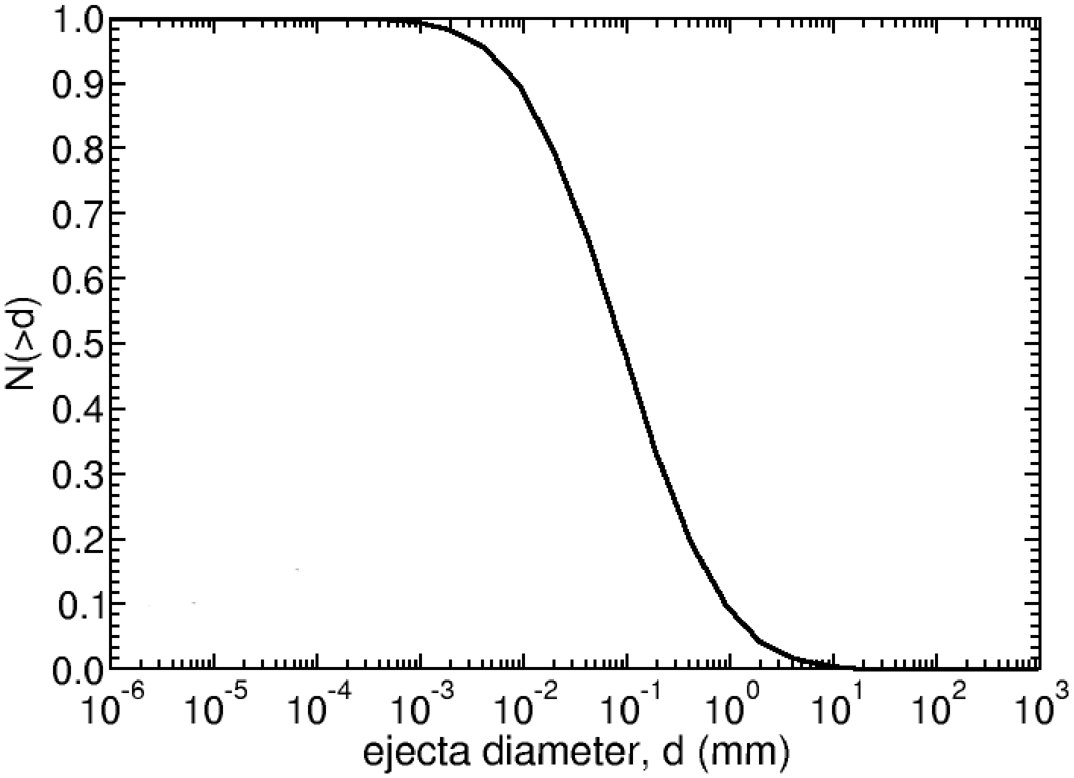

Figure 3.10. The plot shows the total number distribution of ejected particle sizes for lunar soil. The number of particles N that have a diameter equal or greater than d versus the diameter d (mm) [5].

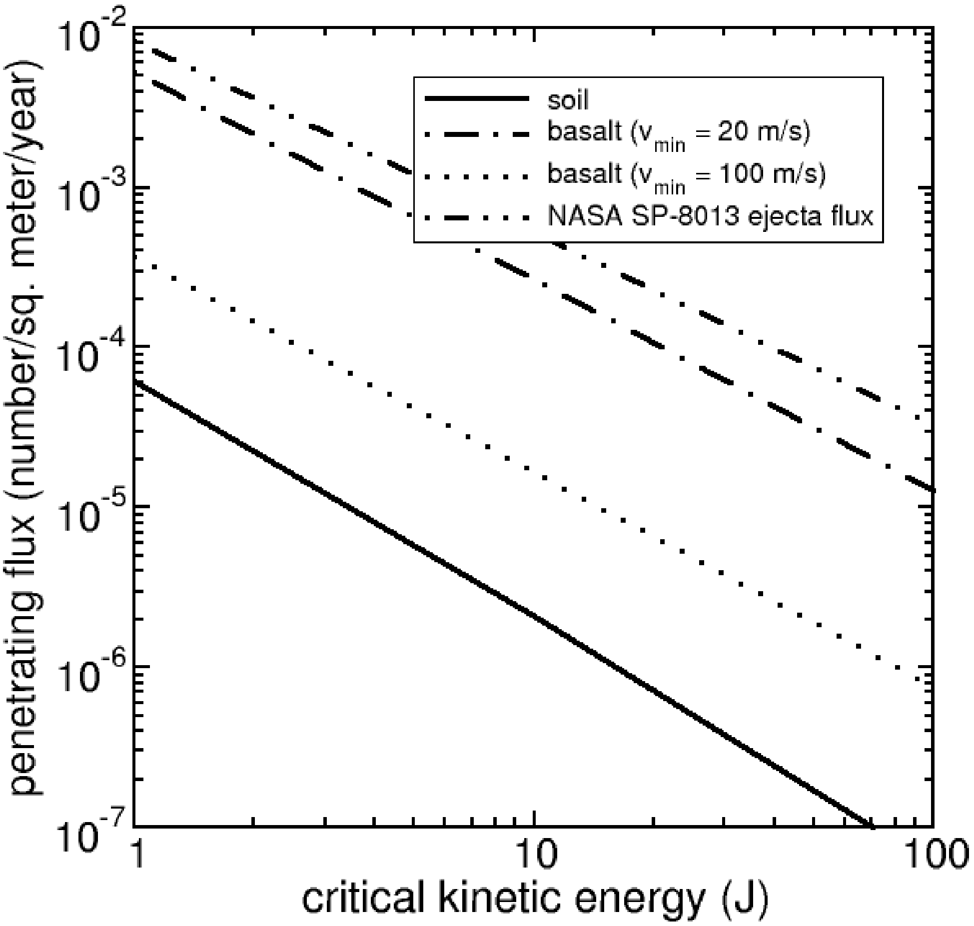

Figure 3.11. The plots show the penetrating flux ($number/(m^2 \cdot year)$) versus the critical kinetic energy (J), which is the energy that should have a particle for penetrate the suit of the astronaut. This shows that the risk of penetration is smaller for the ejecta from lunar soil than the ones from basalt slab, with a reduction factor of 6 to 12 [5].

Chapter 4

Sensor trade-off and simulations

4.1 Measurement advices for impact identification

For monitoring the integrity of the panel the following impact phenomena have been considered:

- Creation of an hole or a crater, which shape is linked to its velocity, direction and material for the impactor and the target[25];
- An high temperature area is generated around the impact region due to the dissipation of energy, with the possible creation of plasma [7];
- Light emission due to the dissipation of energy and creation of plasma [26];
- Vibrational and sound (with atmosphere) waves are generated;
- Creation of debris clouds due to fragmentation of the panel[1].

In addition, the identification of cracks or density variation are taken into account for monitoring internal integrity, not only external one. In the following section, it will be described different measurement advices since their operation, architecture and state of art, when present. The choice will be taken considering relevance of project aim, implementation feasibility, state of art and technological maturity, power and data consumption, materials needed, ISRU approach, development and implementation cost and times.

4.1.1 Electrical Resistivity Imaging (ERI)

This technique is useful for studying cracks and holes of soil in civil context. Thanks to a dedicated software that converts the output voltage, it is possible to display a vertical cross-section picture (figure 4.1) of the electrical properties of the ground. This passage is called “inversion method”. The ERI technique consists of an array of electrodes embedded in the ground, which measure the electric potential difference given an input direct electric current. The array's configuration allows for obtaining a 1D, 2D or 3D image of the subsurface soil. If there is a fracture of the soil, it is possible to measure a change of potential due to the variation of resistivity of the material in the cracks, like air in the case of Earth applications that gives a high value. The total resistivity is an "apparent resistivity" in case of heterogeneous material considered like a homogeneous equivalent medium. Apparent resistivity is calculated following this formula:

$$\rho_{app} = K\frac{\Delta V}{I} \tag{4.1}$$

With ρ_{app} is in $\Omega \cdot m$, I is the added current and ΔV is the measured voltage. While $K = 2\pi \cdot a$ is a geometric coefficient, a is the distance between electrodes; this distance is correlated with the resolution, so the depth, of measurements (up to 1.5 cm)[27].

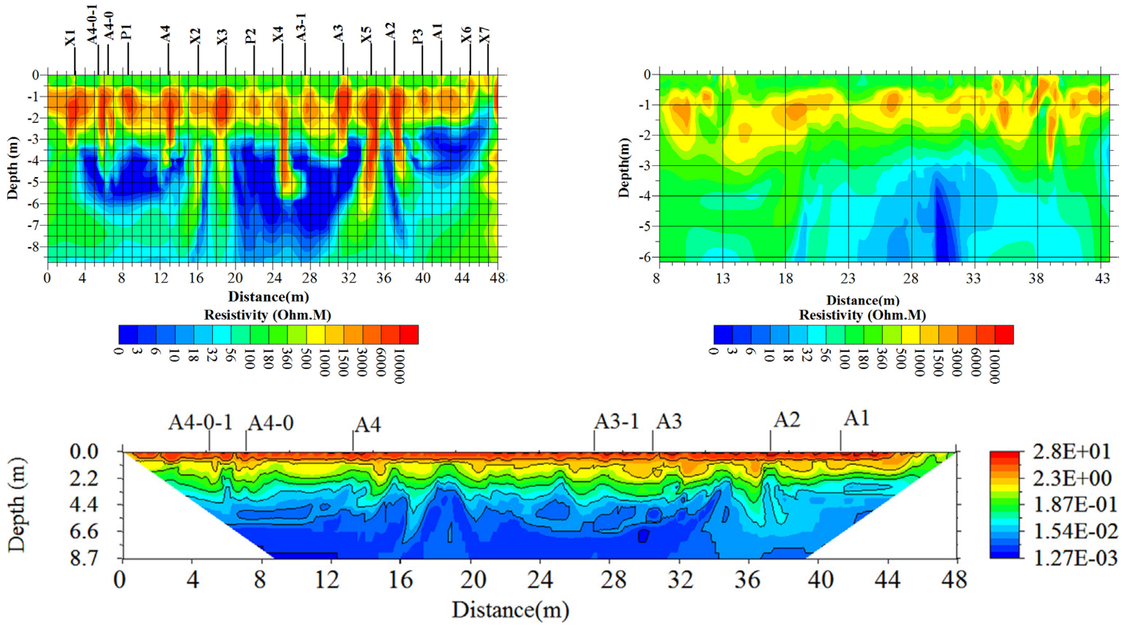

Figure 4.1. Upper images are examples of the pictures that the inversion method generates, starting from an appropriate array of electrodes. The bottom one represents the sensitivity values of the cells used in the inversion model for the Wenner-Schlumberger array [18].

This technique could generate an image of the surface and inner panel given simple information of the degradation and the damage of this element. The challenge is the development of the software for doing the inversion and the power consumption could be very high. In the end, it is important to verify that the electrode material and the panel one are compatible with each other, it is possible to add additive for having a measure that is easier to measure. Nevertheless, ERI remains one of the best methods to address the project issue.

4.1.2 Capacitive sensors for porous matrices

It is possible to consider the panel as a dielectric material in a capacitor, so with electrodes properly positioned the change in value of the dielectric constant could be measured. That variations, or discontinuities, are due to damage or degradation caused by micrometeoroid impacts. For having an easier measurement of this phenomena, an additive material can be mixed with the structural mixture, according with the compatibility of the materials. This possibility represents a novel idea, for which there is no existing research in the state of the art. In literature, capacitive sensors, like Soft Elastomeric Capacitors (SEC), can be used to evaluate cracks and fractures on the surface of metallic or cement elements[35].

So, in this case only the superficial degradation can be measure, not an inner damage.

4.1.3 Resistive Sensors

Examples of the operation of this type of sensors are DEBIE-2 and DRAGONS (respectively [12] and [31]), in fact, in these missions, the sensor relies on the continuity of the conductive lines. Another example is the resistivity sensor developed in Alba CubeSat Unipd project [13].

It can detect sub-millimetric impacts in LEO orbit, but also the position and the dimension of the hole for impacts with dimension of 0.1 mm or more [13].

The continuity of the conductive lines is at the core of its working and the distance between lines is correlated with the resolution of the system. Therefore the control system checks the current flow in each lines, if a line is broken due to an impact there is not current passing through. The electronics detects an open track and updates about the occurrence of an impact. Figure 4.2 represents the functional architecture of a resistivity sensor and control path. With a properly configuration of the sensitive layers, it is possible to evaluate the dimensions and the velocity of the impactor, but also the shape of the crater.

This solution could be applied to the surface of the lunar panel to monitor its surface degradation, but it is necessary to have internal sensors for detecting inner damage.

4.1.4 Traceable markers detectable by Event Camera

Optic sensor can be utilized for tracking light variation, like Event Camera (EC), Neuromorphic Camera or Dynamic Vision Sensor (DVS).

An Event Camera does not make photos like a traditional photographic camera, but it collects circuits of pixels detecting the light variation. These changes are update like binary events, so only the pixels that detect them transmit the information, facilitating latency operations, like in figure 4.3.

Respect to traditional camera, the EC has lots of advantages like:

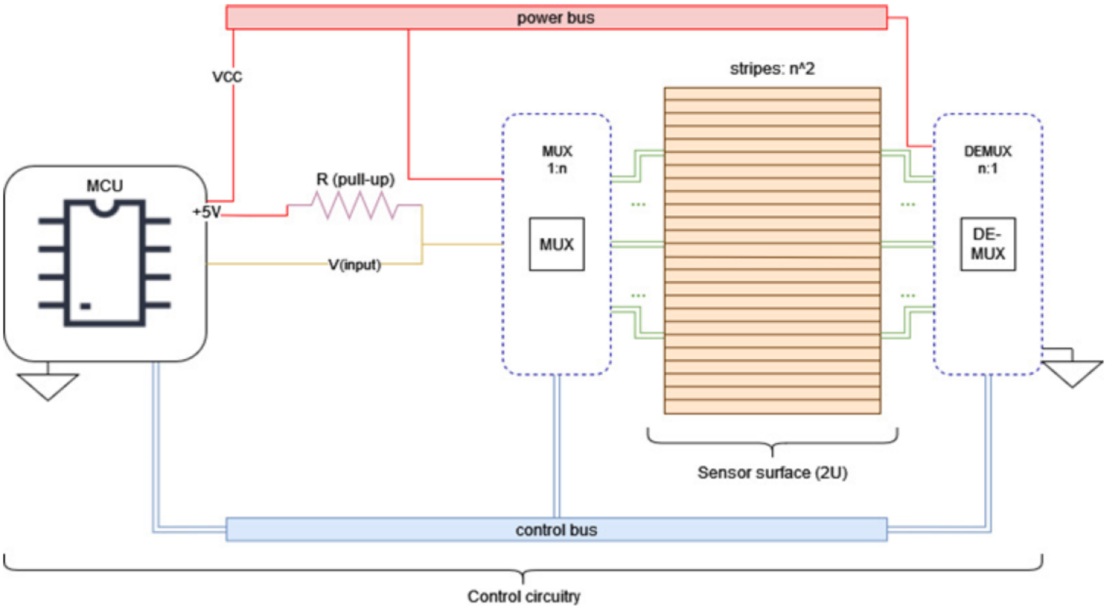

Figure 4.2. In this figure it is represent the functional architecture of a resistivity sensor and control path.

- Temporal resolution of 1 µs, equivalent to 100 000 photograms per second;
- High dynamic range up to 120 dB;
- Over and underexposure are irrelevant;
- Motion blur is irrelevant.

This type of camera is useful in environments with abrupt lighting changes, in fact the EC was tested on the ISS [14].

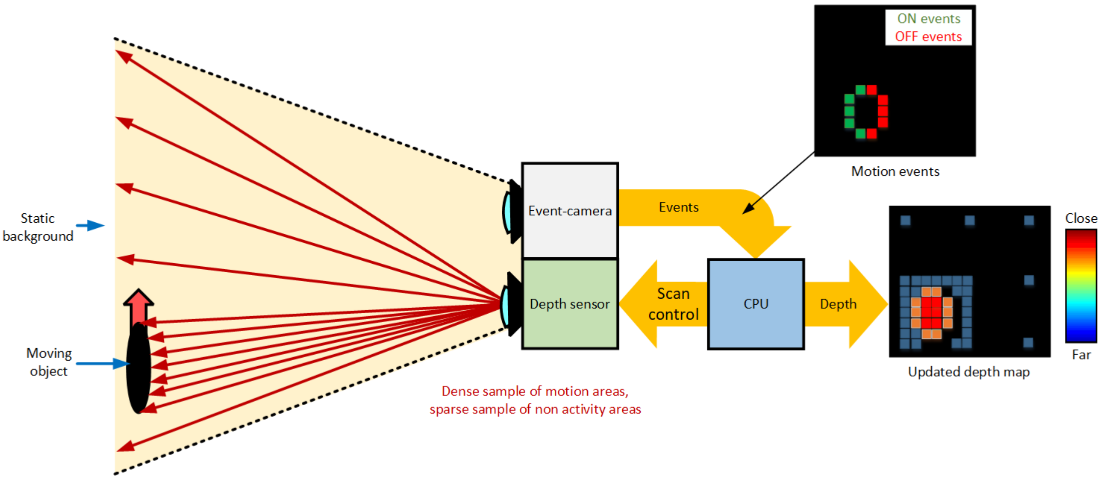

Figure 4.3. An Event Camera and how it works are shown in this figure [16].

For this project the impact could be detect by an EC, but the event might be faint, so it is necessary to amplify the light or the colour with some additives:

- Pigments: coloured compounds derived from algae or other plant organisms;
- Chemiluminescent compounds: with a catalyst some substances could emit light with different wave-length, an example is Luminol reacting with blood or urine [24];
- Phosphorescent compounds: in response to an electronic excitation due to exposure to light source, some substances emit photons, like phosphor;
- Triboluminescent compounds: after a mechanical stress, like impacts, some substances emit light. An example is sugar crystal;
- Pyrotechnics compounds: mixtures emit light after combustion reactions, like Flash Powder composed of potassium perchlorate and aluminium powder.

This solution might be associated with a RADAR technology to detect holes created by impacts and it is necessary to perform thermal control of the instrumentation.

4.1.5 Temperature sensors

As mention before, the impact release energy in form of heat, so a high temperature area is generated around the impact zone. For this reason an array of temperature sensors, like thermocouples, embedded in the panel could measure the variation of temperature. The distance among sensors is relevant for the resolution of the measurement advice. Thanks to the collected data, it is possible to reconstruct an image of the panel using suitable software and a model, which demands a significant amount of computational and energy resources.

Simulations have been conducted to observe this phenomenon, they are reported in the following section. The conclusion is that this solution is not applicable, because the variation of temperature, caused by secondary impacts, is high near the hole, but after a few millimetres it’s no longer appreciable.

4.1.6 Vibration sensors

Piezoelectric sensors could be used for detecting the impact vibrations that propagate trough the panel. Thanks to an appropriate array of these sensors, it is possible to estimate the position and the energy of the impact.

In literature, similar solution have been utilized for detecting debris impacts on aluminium slabs [12].

4.2 Sensors conclusion

In this preliminary phase, the advantages and disadvantages of all these type of sensors have been taken into account, they are summarized in table 4.1.

At the end, ERI, resistive sensors and Event Camera are the best choice in terms of feasibility, technological maturity, power consumption, development of the software and compliance with the mission objectives (monitoring integrity of the panel).

The **resistive sensors** do not require high power and computational resources, also they could detect sub-millimetric holes from heritage. For a superficial analysis they are a valid alternative.
In addition, it is under investigation to use this sensor for studying SPE and GCR particles.

The **EC** can capture information about the surface and detect degradation due to secondary impact. Simulations have determined that the secondary debris can't penetrate the panel completely, but only for few tenths of millimetres.

For evaluate easily the impact with these type of sensors, also with ERI, it is necessary to add elements to the main panel mixture. These additives should be create *in-situ*, according with one of the objectives of this project. It is important to assess the possibility of astronauts being able to create these additives, or tracking agents, *in-situ*.

Measurement Advices	Feasibility	Technological Maturity	Power Required	Software Develop-ment	ISRU Approach	Compatibility with mission purpose
ERI	pro	pro	cons	cons	not specify	pro
Capacitive Sensors	in the middle	cons	cons	cons	not specify	pro
Resistive Sensors	pro	in the middle	pro	pro	not specify	in the middle
Event Camera	not specify	pro	in the middle	pro	in the middle	in the middle
Temperature Sensors	pro	in the middle	in the middle	in the middle	not specify	cons
Vibration Sensors	pro	in the middle	cons	cons	not specify	in the middle

Table 4.1. The main characteristics for each sensor are summarized in this table, with the description of the pros and cons for each type of sensor with regard to feasibility, technological maturity, power required, software development, ISRU approach, compatibility with mission purpose.

4.3 Ansys AUTODYN

The simulations have been performed using Ansys AUTODYN[1] software for modelling impacts between debris and the panel software. ANSYS is a simulation software for non-linear 2D and 3D dynamics that use finite difference, finite volume and finite element techniques, for supporting the engineer in predicting many phenomena, for examples mechanical, fluid dynamic or structural ones. In our case, the phenomenon is similar to fluid dynamic one, because of the high velocity of the impact. A material subjected to a velocity greater than 3 km/s (hypervelocity impact) reacts like a fluid instead of solid material, so for primary and secondary impacts the Smooth Particle Hydrodynamics (SPH) model has been used [2]. In fact, this processor models the elements with lots of little particle elements, not with a mesh. Lagrange and Euler model are implemented in AUTODYN, but they are not able to properly describe that event:

- Lagrange model are not accurate for excessive material deformation, in fact for large deformation in a short period of time this method is not stable. Thus Lagrange is efficient for continuous solid material with continuous structural properties, because the mesh deforms along with the material for small distortions, like in figure 4.4;
- Euler method can be utilized for simulate the behaviour of fluid structures, gaseous material and interaction problems between them. It is useful for large deformations of gaseous material, not for a solid porous panel.

Arbitrary Lagrange Euler (ALE) processor is included in AUTODYN, which is for flow models, it is a Lagrange extension and it gives better results than Lagrange and Euler.

All these processors use explicit time integration and libraries of material data are included.

4.4 Smooth Particle Hydrodynamics - SPH

SPH is the processor chosen to model our phenomenon, thanks to the fact that [29]:

- It is a gridless technique, it doesn't require a numerical grid
    - Respect to Lagrange processor, no grid tangling problems are evaluate;

---

[1] AUTODYN is a trademark of Century Dynamics, Inc., © Copyright 2005 Century Dynamics Inc. All Rights Reserved, Century Dynamics is a subsidiary of ANSYS Inc. AUTODYN® Explicit Software for Nonlinear Dynamics.

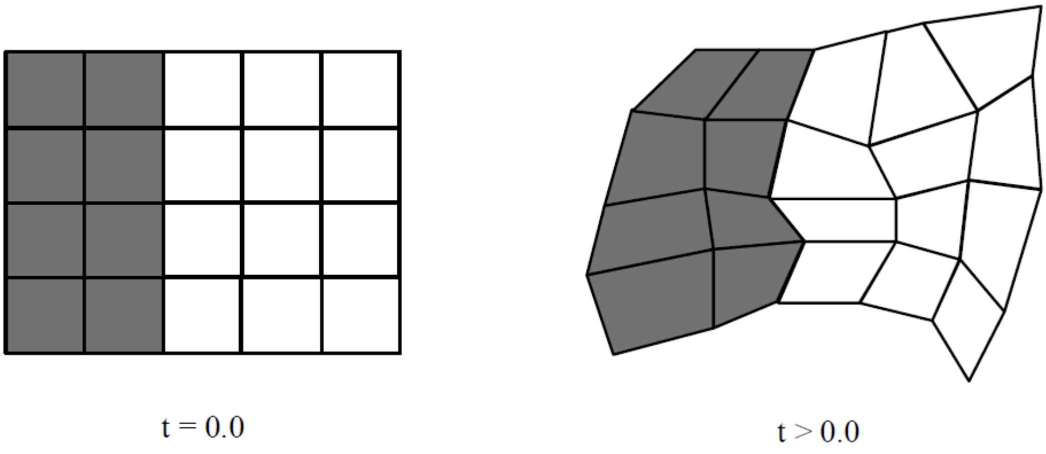

Figure 4.4. A 2D representation of the behaviour of Lagrange mesh after deformation [32].

  - A value for erosion is not require for having correct results, where the term "erosion" refers to the removal of extremely distorted elements;

- It tracks properly the deformation of material and history dependant behaviour;

- Only the regions filled with material are model, not the region in which the material will flow like in Euler processor;

- Respect to Eulerian approach, complex model could be included with relative simplicity

The SPH particles are interpolation points from which values of functions and their derivates can be estimates at discrete points in the continuum. These discrete points, at which quantities are evaluated, are positioned at the centre of the SPH particles.

The parameter called “Particle Size” refers to the diameter of each particle, this value defines the number of particles that can fit into the element. For having a correct simulation, it is important to have 15 or 20 particles along the smaller dimension. In figure 4.5 there are examples of the SPH geometry and it is possible to observe the presence of particles.

4.5 AUTODYN material modelling

To express the conservation of mass, momentum and energy the software uses differential equations for unsteady dynamic motion. It is necessary to relates stress, deformation and internal energy or temperature, at the end the Equations Of State are obtain (EOS). Some EOSs are implemented into AUTODYN [32].

In hypervelocity impacts, strength could be considered negligible because of high stress levels produced.

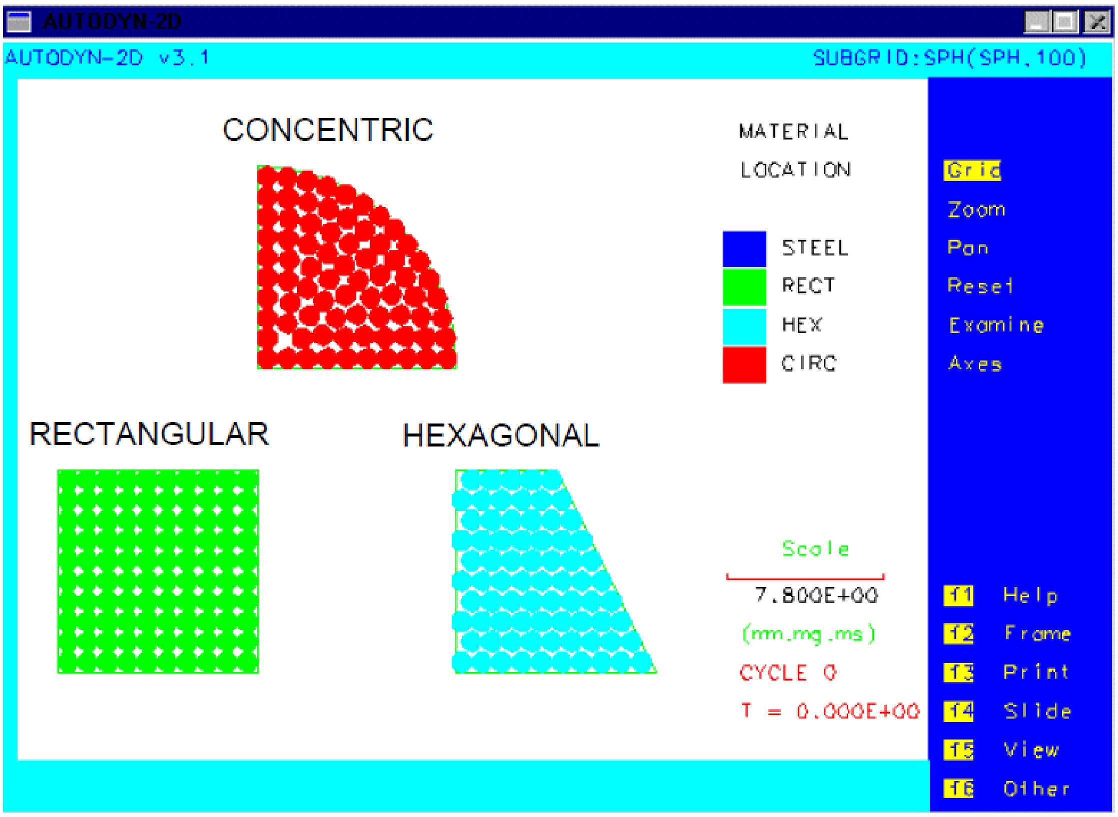

Figure 4.5. A 2D representation of geometric shape for particles and their dimension [29].

Also in porous material, that is the model for the lunar panel, shocks wave are attenuated and the pressure is mitigated thank to the pores. The porous material compacts to its solid state and a large amount of energy is absorbed by the fracture of the holes, releasing heat and creating a high temperature area.

For these reasons, P-α model has been used for modelling the material of panel. It is a phenomenological approach for giving the correct behaviour of porous material at high stresses and compaction process at low stresses. The main assumption is to have the same specific energy for porous material as for solid one, at the same pressure and temperature. The parameter α is the porosity, calculated as:

$$\alpha = \left(\frac{V}{V_s}\right) \tag{4.2}$$

Where V is the specific volume of porous element and V_s is the specific volume of the solid state, at same pressure and temperature [32].

The behaviour of porous element is shown in figure 4.6, the material is elastic up to a pressure P_e, then it is plastic until the fully compaction at pressure P_s, where the material is in its solid state.

In next section, the values used for modelling during the simulations and the simu-

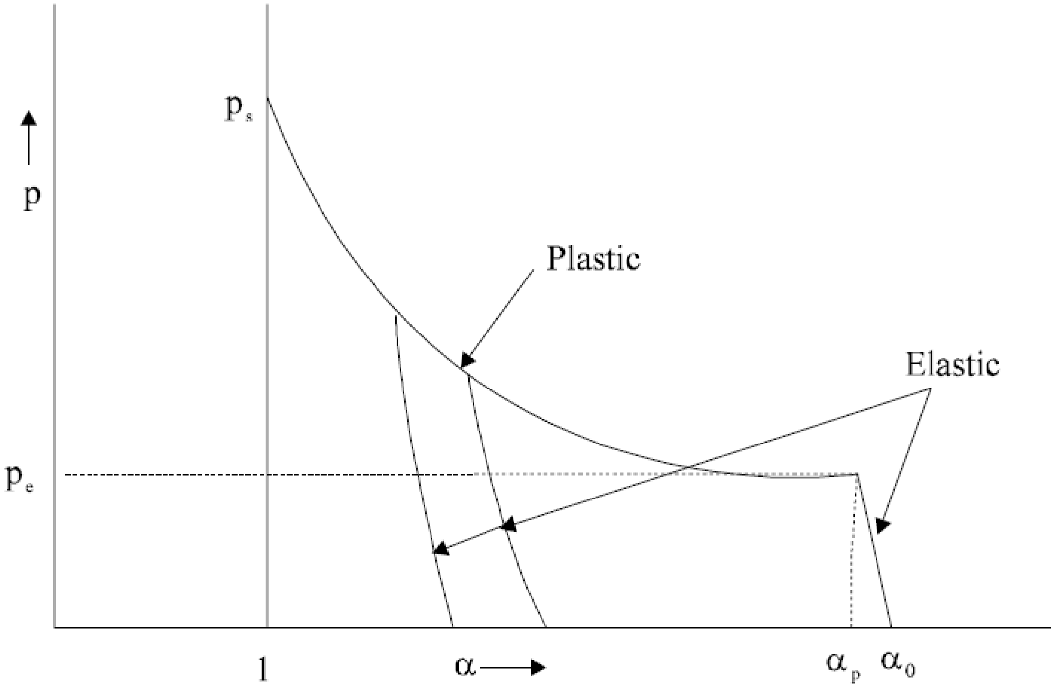

Figure 4.6. The behaviour of porous material in function of pressure versus α parameter is shown in this figure [32].

lations will be described.

4.6 Simulations

The purpose of the simulations is to clarify the variation of temperature for the choice or not of the temperature sensors. For a preliminary analysis, **concrete** has been chosen as material for modelling the impactor and the target (respectively the ejecta or primary particle and the lunar panel). Given that the final purpose is to create a panel with variation in porosity, the outer part has been considered solid, therefore the material does not need to be highly porous. This material is already implemented in the AUTODYN library with P-α model, so **concrete – 35 MPa** was chosen for its density value, the one most similar to the density of lunar regolith compared to other materials available in the library. In figure 4.7, the characteristics of concrete – 35 MPa are reported.

The projectile is round and the target has a rectangular shape, the simulations have 2D design to limit the computational cost, figure 4.8. In the table 4.2 are summarized the values for both projectile and target.

For SPH model the Particle size has the value of 5.6×10^{-3}mm, resulting 18 particles along the smaller dimension that is the diameter of the projectile, as in figure 4.9.

With a total of 148 SPH nodes for projectile and 80 000 SPH nodes for target.

	Projectile, ejecta	**Panel**
Diameter	100 µm	—
Thickness	—	1 mm
Material	Concrete - 35MPa	Concrete - 35MPa
Velocity	1 000 m/s	0 m/s

Table 4.2. The parameters of projectile and panel used in simulations are tabulated here.

In conclusion, for a concrete ejecta particle with a speed of 1 km/s that impacts against a concrete target, which has zero velocity, the variation of temperature is negligible already at few tenths of millimetre away from the impact area, as shown in figure 4.10. So sensor of temperature has been discarded during this phase of the project.

For having a correspondence of the ejecta velocity value, a simulation of an impact between a primary debris and the panel has been done, the values are reported in table 4.3. Resulting that the ejecta velocity, from a 13 300 m/s impact, is about $8{,}6\times10^{-3}$ m/s and a thickness of 20 mm prevents the perforation of the concrete panel, see figure 4.11.

	Projectile, primary	**Panel**
Diameter	4 mm	—
Thickness	—	20 mm
Material	Concrete - 35MPa	Concrete - 35MPa
Velocity	13 300 m/s	0 m/s

Table 4.3. The parameters of projectile and panel used in the simulation of a primary impact are tabulated here.

The "new" projectile dimensions are of few millimetres instead of few micro-meter, owing to a simulation error caused by the restricted value of particle size for SPH coupled with a large number of particle into the slab.

It is possible to achieve that the real total velocity would be less than the one simulated.

This result differs from that of Donald experiments (velocity of 0.5 km/s), because Donald conducted his tests using an aluminium projectile against a basalt slab, whereas ours simulations are based on a concrete or basalt projectile. The choice of these materials better simulates the debris that could potentially impact the lunar surface or the lunar panel. Therefore, due to the low velocity of the ejecta, we can conclude that panel perforation does not occur.

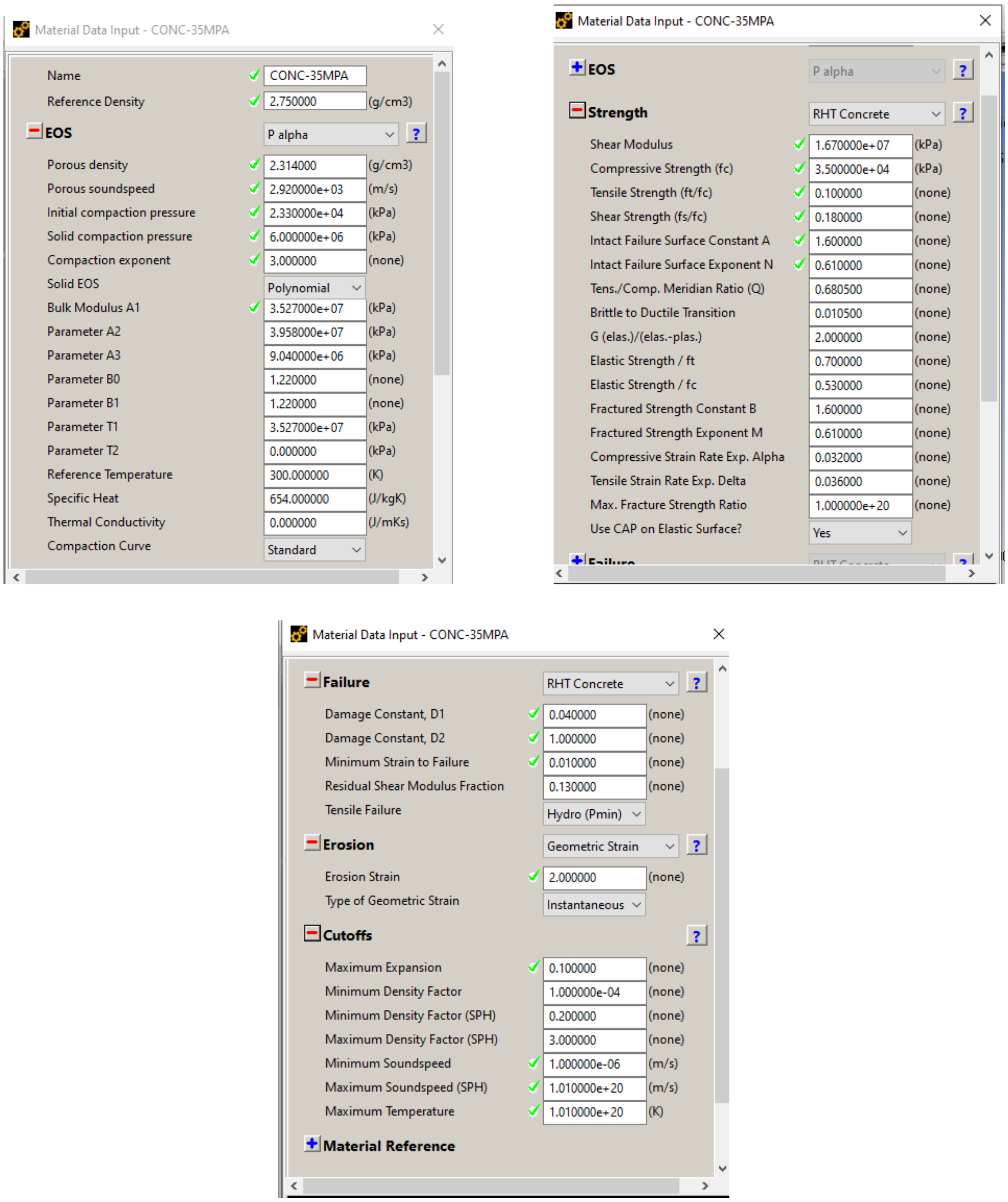

Name	✓	CONC-35MPA	
Reference Density	✓	2.750000	(g/cm3)
EOS		P alpha	
Porous density	✓	2.314000	(g/cm3)
Porous soundspeed	✓	2.920000e+03	(m/s)
Initial compaction pressure	✓	2.330000e+04	(kPa)
Solid compaction pressure	✓	6.000000e+06	(kPa)
Compaction exponent	✓	3.000000	(none)
Solid EOS		Polynomial	
Bulk Modulus A1	✓	3.527000e+07	(kPa)
Parameter A2		3.958000e+07	(kPa)
Parameter A3		9.040000e+06	(kPa)
Parameter B0		1.220000	(none)
Parameter B1		1.220000	(none)
Parameter T1		3.527000e+07	(kPa)
Parameter T2		0.000000	(kPa)
Reference Temperature		300.000000	(K)
Specific Heat		654.000000	(J/kgK)
Thermal Conductivity		0.000000	(J/mKs)
Compaction Curve		Standard	

EOS		P alpha	
Strength		RHT Concrete	
Shear Modulus	✓	1.670000e+07	(kPa)
Compressive Strength (fc)	✓	3.500000e+04	(kPa)
Tensile Strength (ft/fc)	✓	0.100000	(none)
Shear Strength (fs/fc)	✓	0.180000	(none)
Intact Failure Surface Constant A	✓	1.600000	(none)
Intact Failure Surface Exponent N	✓	0.610000	(none)
Tens./Comp. Meridian Ratio (Q)		0.680500	(none)
Brittle to Ductile Transition		0.010500	(none)
G (elas.)/(elas.-plas.)		2.000000	(none)
Elastic Strength / ft		0.700000	(none)
Elastic Strength / fc		0.530000	(none)
Fractured Strength Constant B		1.600000	(none)
Fractured Strength Exponent M		0.610000	(none)
Compressive Strain Rate Exp. Alpha		0.032000	(none)
Tensile Strain Rate Exp. Delta		0.036000	(none)
Max. Fracture Strength Ratio		1.000000e+20	(none)
Use CAP on Elastic Surface?		Yes	

Failure		RHT Concrete	
Damage Constant, D1	✓	0.040000	(none)
Damage Constant, D2	✓	1.000000	(none)
Minimum Strain to Failure	✓	0.010000	(none)
Residual Shear Modulus Fraction		0.130000	(none)
Tensile Failure		Hydro (Pmin)	
Erosion		Geometric Strain	
Erosion Strain	✓	2.000000	(none)
Type of Geometric Strain		Instantaneous	
Cutoffs			
Maximum Expansion	✓	0.100000	(none)
Minimum Density Factor		1.000000e-04	(none)
Minimum Density Factor (SPH)		0.200000	(none)
Maximum Density Factor (SPH)		3.000000	(none)
Minimum Soundspeed	✓	1.000000e-06	(m/s)
Maximum Soundspeed (SPH)	✓	1.010000e+20	(m/s)
Maximum Temperature	✓	1.010000e+20	(K)
Material Reference			

Figure 4.7. The values of concrete - 35MPa used during simulations.

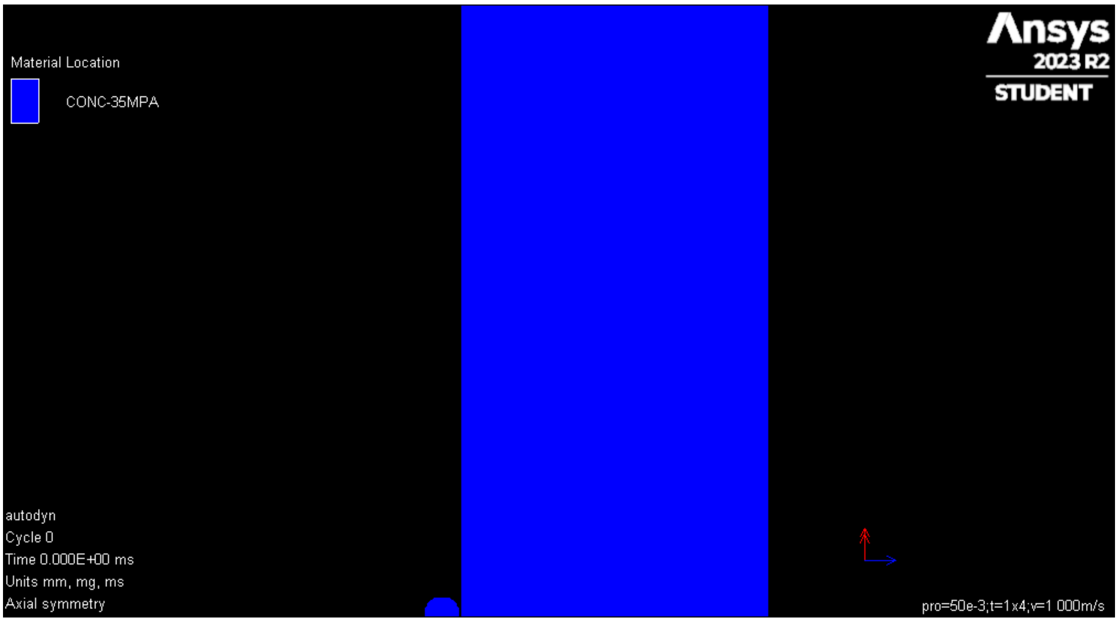

Figure 4.8. The round projectile and the target are represented, both fill with concrete - 35MPa.

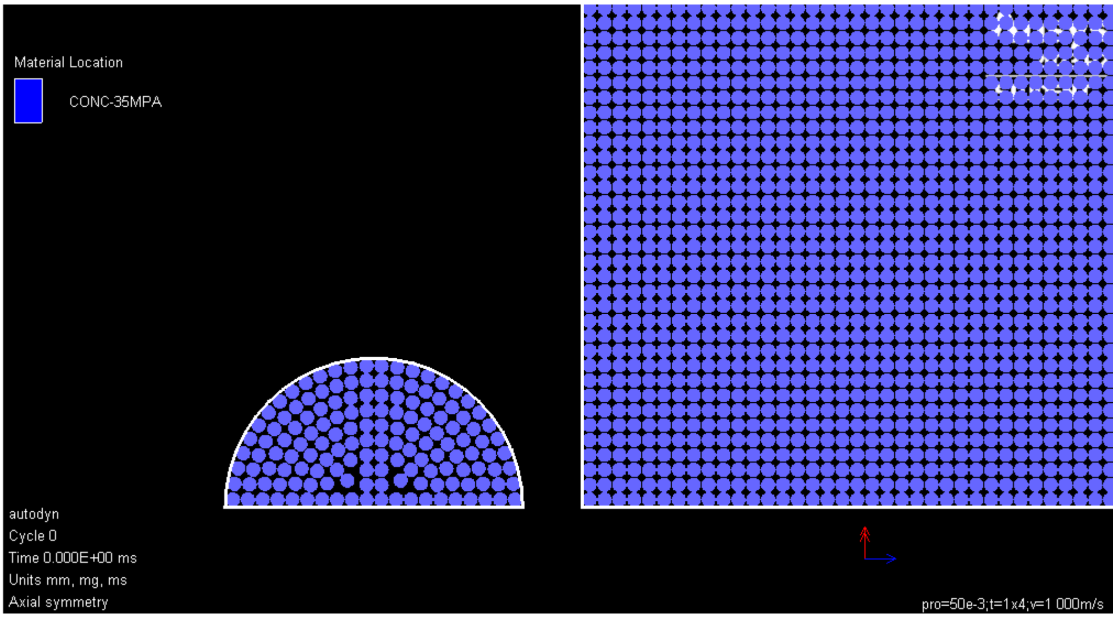

Figure 4.9. SPH particles representation filling both projectile and target.

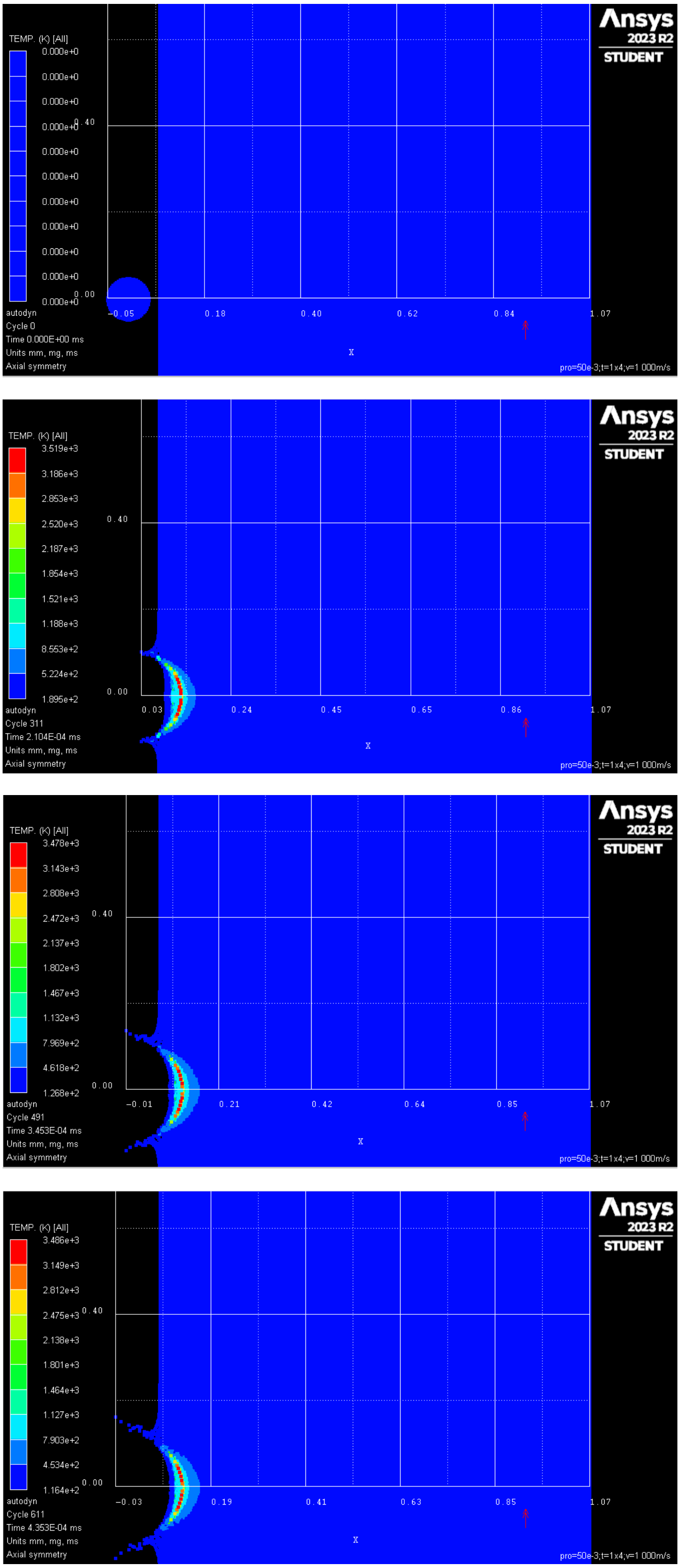

Figure 4.10. This simulation evaluates that the variation of temperature is negligible already at few tenths of millimetre away from the impact area.

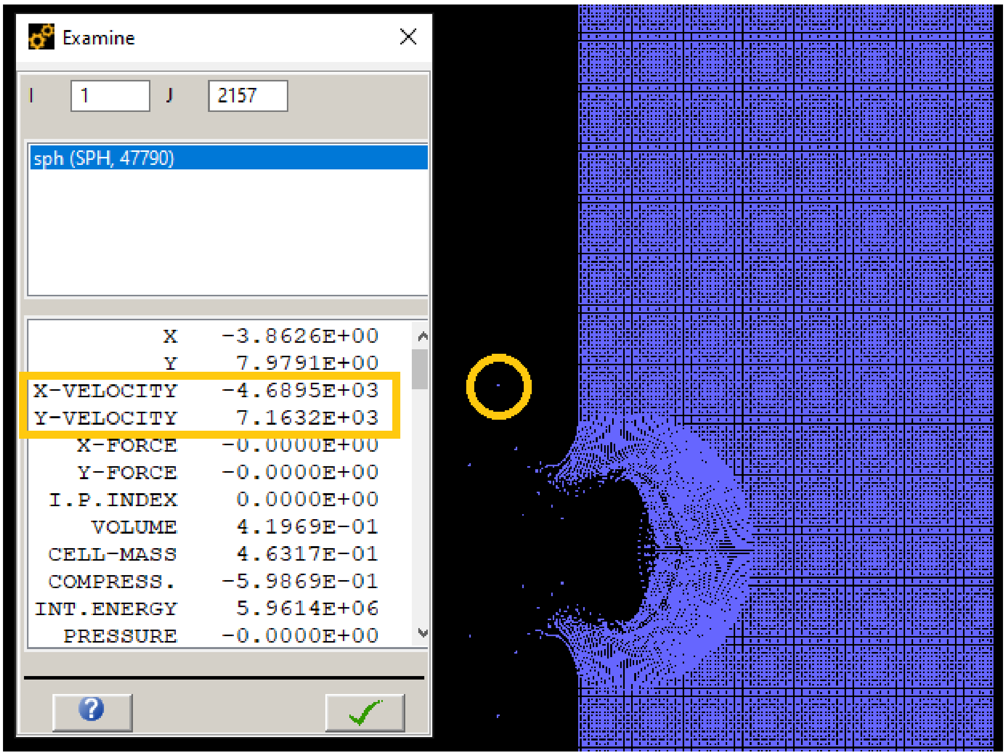

```
I  1    J  2157
sph (SPH, 47790)
            X    -3.8626E+00
            Y     7.9791E+00
   X-VELOCITY    -4.6895E+03
   Y-VELOCITY     7.1632E+03
      X-FORCE    -0.0000E+00
      Y-FORCE    -0.0000E+00
   I.P.INDEX      0.0000E+00
       VOLUME     4.1969E-01
    CELL-MASS     4.6317E-01
    COMPRESS.    -5.9869E-01
   INT.ENERGY     5.9614E+06
     PRESSURE    -0.0000E+00
```

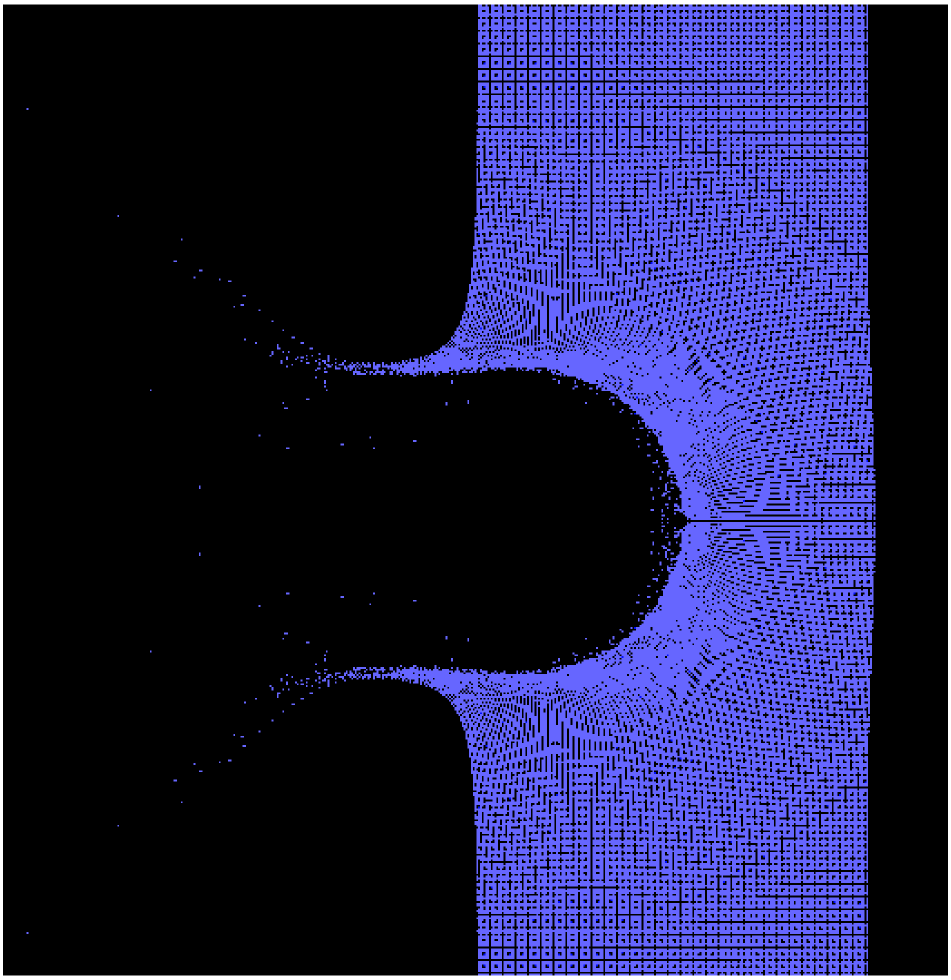

Figure 4.11. These simulation represents the impact of a 13 300 m/s projectile against a slab, both materials are concrete. The upper figure shows the properties of a selected particle (ejecta particle), the most important values for our application are the components of the velocity, getting a total velocity less than 0.5 km/s. The other figure represents the no-perforation of a slab with a thickness of 20 mm.

Chapter 5

Conclusions and Future developments

Studies on lunar regolith simulant are going on in future months, also test for 3D-printed panels and for foaming the mixture will be done.

The main basic component is LMS-1D to simulate better the lunar regolith, adding elements like metakaoline to have a better configuration of the mixture for the panel.

Analyzing the lunar environment, the characteristics of the panel and the terrestrial technologies, some measurement advices were chosen for monitoring the integrity and the damage of the panel. Electrical Resistivity Imaging, resistive sensors and Event Camera were selected for detecting the impact and the damage caused by a primary or secondary debris against our infrastructure.

ERI technique is the more promising, thanks to the possibility to have an inner vision of the panel and its state, but also because of its technological maturity in civil sector.

The resistive sensors can observe a superficial damage and can evaluate the dimension of the projectile up to tens of millimeters, also they are already used in space. Furthermore, the possibility to measure Solar Particle Events and Cosmic Galaxy Rays radiation is under investigation.

It is necessary to test the compatibility between the component of the advices and the geopolymeric material of the structure, to develop a software for the inversion of ERI imagine, to test the light intensity due to an impact for using the Event Camera, and to test the entire system of measurement.

Of course a future development should be having a better model for the material in Ansys AUTODYN, which should represent basalt or the simulant used for the panel. For this, some mechanical tests are required to evaluate the parameter for the implementation in Autodyn.

References

[1] "A CubeSat-sized in-situ space debris impact sensor". In: 2023, G. Battaglia, S. Enzo, G. Trevisanuto, S. Lopresti, F. Marin, G. Bezze, Dr. Lorenzo Olivieri, F. Basana, Prof. Alessandro Francesconi, 21st IAA SYMPOSIUM ON SPACE DEBRIS.

[2] *ANSYS AUTODYN User's Manual*.

[3] Chengying Bai and Paolo Colombo. "Processing, properties and applications of highly porous geopolymers: A review". In: *Ceramics International* 44.14 (2018), pp. 16103–16118. ISSN: 0272-8842. DOI: https://doi.org/10.1016/j.ceramint.2018.05.219. URL: https://www.sciencedirect.com/science/article/pii/S0272884218313610.

[4] Chengying Bai, Alberto Conte, and Paolo Colombo. "Open-cell phosphate-based geopolymer foams by frothing". In: *Materials Letters* 188 (2017), pp. 379–382. ISSN: 0167-577X. DOI: https://doi.org/10.1016/j.matlet.2016.11.103. URL: https://www.sciencedirect.com/science/article/pii/S0167577X16318523.

[5] Michael D. Bjorkman and Eric L. Christiansen. "An Astronaut's Risk of Experiencing a Critical Impact from Lunar Ejecta during Lunar EVA". In: (2019). URL: https://ntrs.nasa.gov/citations/20190033488.

[6] Papa E. et al. "K2O-Metakaolin-Based Geopolymer Foams: Production, Porosity Characterization and Permeability Test." In: *Materials (Basel)* 15(3):1008 (2022), pp. –-. ISSN: 0167-577X. DOI: https://doi.org/10.3390/ma15031008. URL: https://pubmed.ncbi.nlm.nih.gov/35160953/.

[7] G. Eichhorn. "Analysis of the hypervelocity impact process from impact flash measurements". In: *Planetary and Space Science* 24.8 (1976), pp. 771–781. ISSN: 0032-0633. DOI: https://doi.org/10.1016/0032-0633(76)90114-8. URL: https://www.sciencedirect.com/science/article/pii/0032063376901148.

[8] D. E. Gault, H. J. Moore, and Shoemaker. *Spray Ejected from the Lunar Surface by Meteoroid Impact*. Tech. rep. NASA, 1963.

[9] Felix Horst et al. "Thick shielding against galactic cosmic radiation: A Monte Carlo study with focus on the role of secondary neutrons". In: *Life Sciences in Space Research* 33 (Apr. 2022). DOI: 10.1016/j.lssr.2022.03.003.

[10] Friedrich Hörz et al. *LUNAR SURFACE PROCESSES*. Cambridge University Press, 1991. Chap. 4. URL: https://www.lpi.usra.edu/publications/books/lunar_sourcebook/.

[11] Kevin Housen, Robert Schmidt, and Keith Holsapple. "Crater ejecta scaling laws: Fundamental forms based on dimensional analysis". In: *Journal of Geophysical Research* 88 (Apr. 1983). DOI: 10.1029/JB088iB03p02485.

[12] "In-Flight and Post-Flight Impact Data Analysis from DEBIE2 (Debris In-Orbit Evaluator) on Board of ISS". In: 2013, Menicucci Alessandra, Drolshagen Gerhard, Kuitunen Juha, Butenko Yuriy, Mooney Cathal, 6th European Conference on Space Debris.

[13] "AlbaSat: an educational satellite for a multi-objective mission in LEO". In: 2023, L. Lion, G. Basana, G. Battaglia, F. Berra, S. Enzo, M. Mozzato, L. Guglielmini, R. Lazzaro, L. Nuti, L. Olivieri, A. Stanco, A. Francesconi, E2. 51st IAF STUDENT CONFERENCE, IAC-23.

[14] Matthew G. McHarg et al. "Falcon Neuro: an event-based sensor on the International Space Station". In: *Optical Engineering* 61.8 (2022), p. 085105. DOI: 10.1117/1.OE.61.8.085105. URL: https://doi.org/10.1117/1.OE.61.8.085105.

[15] David S. McKay et al. *THE LUNAR REGOLITH*. Cambridge University Press, 1991. Chap. 7. URL: https://www.lpi.usra.edu/publications/books/lunar_sourcebook/.

[16] Manasi Muglikar, Diederik Paul Moeys, and Davide Scaramuzza. "Event Guided Depth Sensing". In: Dec. 2021. DOI: 10.1109/3DV53792.2021.00048.

[17] NASA. *Moon Facts*. URL: https://science.nasa.gov/moon/facts/. accessd: 02.2024.

[18] Ahmad Neyamadpour. "Detection of subsurface cracking depth using electrical resistivity tomography: A case study in Masjed-Soleiman, Iran". In: *Construction and Building Materials* 191 (2018), pp. 1103–1108. ISSN: 0950-0618. DOI: https://doi.org/10.1016/j.conbuildmat.2018.10.027. URL: https://www.sciencedirect.com/science/article/pii/S0950061818324255.

[19] Shima Pilehvar et al. "Utilization of urea as an accessible superplasticizer on the moon for lunar geopolymer mixtures". In: *Journal of Cleaner Production* 247 (2020), p. 119177. ISSN: 0959-6526. DOI: https://doi.org/10.1016/j.jclepro.2019.119177. URL: https://www.sciencedirect.com/science/article/pii/S0959652619340478.

[20] Shima Pilehvar et al. "Investigation of severe lunar environmental conditions on the physical and mechanical properties of lunar regolith geopolymers". In: *Journal of Materials Research and Technology* 11 (2021), pp. 1506–1516. ISSN: 2238-7854. DOI: https://doi.org/10.1016/j.jmrt.2021.01.124. URL: https://www.sciencedirect.com/science/article/pii/S2238785421001241.

[21] Jeff Plescia. *Lunar Regolith – Understanding for Science and Exploration*. URL: https://www.hou.usra.edu/meetings/leag2016/presentations/Wednesday/plescia.pdf.

[22] John L. Provis. "Alkali-activated materials". In: *Cement and Concrete Research* 114 (2018). Report of UNEP SBCI WORKING GROUP ON LOW-CO2 ECO-EFFICIENT CEMENT-BASED MATERIALS, pp. 40–48. ISSN: 0008-8846. DOI: https://doi.org/10.1016/j.cemconres.2017.02.009. URL: https://www.sciencedirect.com/science/article/pii/S0008884616307700.

[23] P. Raju. "Advances in manufacture of Mooncrete – a Review". In: *International Journal of Engineering Science and Advanced Technology* 4 (Nov. 2014), pp. 501–510.

[24] Ramsthaler. "Duration and intensity of chemiluminescence of different luminol kits." In: *Rechtsmedizin* 27 (2017), pp. 185–190. DOI: https://doi.org/10.1007/s00194-017-0150-5.

[25] Paul R. Ratcliff et al. "Experimental measurements of hypervelocity impact plasma yield and energetics". In: *International Journal of Impact Engineering* 20.6 (1997). Hypervelocity Impact, pp. 663–674. ISSN: 0734-743X. DOI: https://doi.org/10.1016/S0734-743X(97)87453-2. URL: https://www.sciencedirect.com/science/article/pii/S0734743X97874532.

[26] Si-yuan Ren et al. "Satellite breakup behaviors and model under the hypervelocity impact and explosion: A review". In: *Defence Technology* 27 (2023), pp. 284–307. ISSN: 2214-9147. DOI: https://doi.org/10.1016/j.dt.2022.08.004. URL: https://www.sciencedirect.com/science/article/pii/S2214914722001702.

[27] A. Samouëlian et al. "Electrical Resistivity Imaging for Detecting Soil Cracking at the Centimetric Scale". In: *Soil Science Society of America Journal - SSSAJ* 67 (Sept. 2003). DOI: 10.2136/sssaj2003.1319.

[28] Emerson Speyerer et al. "Quantifying crater production and regolith overturn on the Moon with temporal imaging". In: *Nature* 538 (Oct. 2016), pp. 215–218. DOI: 10.1038/nature19829.

[29] *ANSYS SPH User Manual and Tutorial, Revision 4.3 Century Dynamics*.

[30] *NASA SPACE FLIGHT HUMAN-SYSTEM STANDARD: VOLUME 1: CREW HEALTH*.

[31] "The Space Debris Sensor Experiment". In: 2019, P. Anz-Meador, M. Ward, A. Manis, K. Nornoo, B. Dolan, C. Claunch, J. Rivera, International Orbital Debris (IOC) Conference.

[32] *ANSYS Theory Manual, Revision 4.3, Century Dynamics*.

[33] Vittorio Vanzani, F. Marzari, and E. Dotto. "Micrometeoroid impacts on the lunar surface". In: 28 (Feb. 1997), p. 1481.

[34] Zigong Xu et al. "Primary and albedo protons detected by the Lunar Lander Neutron and Dosimetry experiment on the lunar farside". In: (Sept. 2022), p. 974946. DOI: `10.3389/fspas.2022.974946`.

[35] Jin Yan et al. "Concrete Crack Detection and Monitoring Using a Capacitive Dense Sensor Array". In: *Sensors* 19.8 (2019). ISSN: 1424-8220. DOI: `10.3390/s19081843`. URL: `https://www.mdpi.com/1424-8220/19/8/1843`.

List of Figures

List of Tables